Berry Phase Calculations of the Rotational and Pseudorotational g-factor in Molecules and Solids

Thesis submitted for the degree of
Doctor Philosophiae

CANDIDATE: Davide Ceresoli

SUPERVISOR: Erio Tosatti

October 2002

Contents

Chapter 1

Introduction

Rotations and pseudorotations in molecules and in solids are cyclic motions where the ionic coordinates execute a closed orbit, thus giving rise, in virtue of their bare charge, to an orbital magnetic moment. Electrons however also take part in the motion; and were they to cling infinitely tightly to the ions, they should completely screen – totally cancel – the ionic orbital magnetic moment. In reality, the electrons are only softly tied to the ions, and do not exactly cancel the ionic magnetic moment. The compound result of ion and electron orbital motion is a total rotational g-factor tensor g^R_{ii}, $i = 1, 2, 3$ [1], whose components may take real values, ranging from one (no screening) to zero (perfect screening), to negative (overscreening).

g^R_{ii} is a basic property, long known for rotation of simple molecules such as H_2 [2, 3], but not always quantitatively available, particularly for pseudorotations. The latter may be of special relevance for Jahn-Teller (JT) and pseudo-JT systems in free molecules and in solids, for example those of C_{60} [4], such as those with displacive structural transitions[5, 6, 7], including incipient ferroelectric perovskites[8] and perhaps some special glasses [9, 10, 11, 12].

High-accuracy Hartree-Fock and Multi Configurational Self Consistent Field molecular calculations of rotational g-factors are well established in the chemical literature[1, 13, 14]. Though quite successful, these approaches are not easily extended to solids. On the other hand, the density functional

methods that are standard in both solids and molecules could in principle be straightforwardly extended to calculate the g^R tensor.

The motion of the ions being slow, it can in fact be treated as an adiabatic parameter with respect to the electrons. In presence of a magnetic field, the electrons cause the appearance of an additional geometric vector potential (GVP) which is a Berry connection [15]. The work done in this thesis is aimed at providing a practical and accurate density functional method for evaluating the rotational and pseudorotational g-factor of molecules and solids through a Berry phase technique, as the rotational g-factor is a manifestation of Berry's phase [15, 16, 17, 18].

In chapter 2, we will recall how in presence of an external magnetic field the usual Born-Oppenheimer approximation has to be modified to include a geometric vector potential term acting on the nuclear degrees of freedom. The GVP adds to the magnetic vector potential $\mathbf{A}(\mathbf{R})$; its gradient gives rise to a force which acts to modify, "screen" the Lorentz force due to the bare nuclear charges.

In chapter 3, we will show benchmark results for the g-factor of rotating molecules, where direct physical interpretation of the magnetic screening factor is quite transparent. The results will be compared to experimental data, and to previous quantum-chemical calculations, generally with excellent agreement.

In chapter 4, we will present an alternative implementation, based on a local orbital calculation scheme, including the magnetic field through a "Peierls" phase factors. This method is suitable for a faster, if somewhat less accurate evaluation of the rotational g-factor.

In the second part of this thesis, we will apply our technique to pseudorotations in solids. Motivated by experimental data by Lawless [19], showing a magnetic field dependence of the static dielectric constant of two quantum paraelectrics, potassium tantalate ($KTaO_3$) and strontium titanate ($SrTiO_3$),

we will discuss the possible effects of an external magnetic field on the dielectric response of quantum paraelectrics. We will focus our attention specifically on the Zeeman interaction of the orbital magnetic moment connected with the soft mode, with the external magnetic field. That is expected to yield weak splittings and shifts, which can only be of significance in quantum paraelectrics and incipient ferroelectrics, where the soft mode frequency is very low.

After reviewing in chapter 5 the phenomenology of quantum ferroelectrics and paraelectrics, we will show in chapter 6 results about the pseudorotational g-factor of $KTaO_3$ and $SrTiO_3$. Finally, in chapter 7, we will relate the orbital magnetic moment and the pseudorotational g-factor to the change of static dielectric constant in a magnetic field. The calculated effect is several orders of magnitude smaller than that observed in these incipient ferroelectrics. This suggests that while a different mechanism may be at work in these compounds, a measurement of the rotational g-factor in these systems must await different experiments.

Chapter 2

Theoretical background and computational methods

In this chapter we start by illustrating the theoretical tools used to calculate the electronic structure of the systems under consideration. Using the Born-Oppenheimer (BO) approximation it is possible to decouple the ionic and electronic degrees of freedom thanks to their large mass difference; the BO approximation consist in solving the Schrödinger equation for the electronic ground state by considering the nuclei as fixed. All the calculations are done within the framework of Density Functional Theory (DFT) [20], which is widely used in modern computational materials science. The ground state electronic wavefunction is the starting point for treating the magnetic field within the Density Functional Perturbation Theory (DFPT) [21]. In the following we illustrate the general DFT and DFPT framework in the plane wave implementation. We will show how the BO approximation has to be modified in order to include the magnetic field and the "screening" of the electrons on the nuclear degrees of freedom.

2.1 Density functional theory

The Density Functional Theory describes an electronic system based on a theorem stating that the ground state properties of an interacting electron system is uniquely determined by its electronic density, which minimizes the energy functional [20]:

$$E[n(\mathbf{r})] = F[n(\mathbf{r})] + \int V_{ext}(\mathbf{r})n(\mathbf{r})d\mathbf{r}, \tag{2.1}$$

where V_{ext} in the external potential, $F[n]$ is a universal functional (independent of V_{ext}) and the density $n(\mathbf{r})$ must integrate to N, the number of electrons in the system.

Unfortunately, the functional $F[n]$ is unknown, and all its approximations in terms of the density alone give poor results. In order to transform DFT into a practical tool, Kohn ans Sham (KS) [22] introduced an auxiliary system of non-interacting electrons, with the same density of the original one. In this way the functional $F[n]$ is split into three parts:

$$F[n(\mathbf{r})] = T_s[n(\mathbf{r})] + \frac{1}{2}\int \frac{n(\mathbf{r})n(\mathbf{r}')}{|\mathbf{r}-\mathbf{r}'|}d\mathbf{r}d\mathbf{r}' + E_{xc}[n(\mathbf{r})], \tag{2.2}$$

where T_s is the kinetic energy of the non interacting system, the second term is the classical electrostatic interaction, and the last term, called exchange-correlation energy, accounts for all the many-body effects. The minimization of $F[n]$ imposing the constraint that the integrated density must give the total number of electrons, is equivalent to solving self consistently the following set of equation:

$$H_{KS}\psi_i(\mathbf{r}) = \left[-\frac{1}{2}\nabla^2 + V_{SCF}(\mathbf{r})\right]\psi_i(\mathbf{r}) = \epsilon_i\psi_i(\mathbf{r}), \tag{2.3}$$

$$V_{SCF}(\mathbf{r}) = V_{ext}(\mathbf{r}) + \int \frac{n(\mathbf{r}')}{|\mathbf{r}-\mathbf{r}'|}d\mathbf{r}' + v_{xc}(\mathbf{r}), \tag{2.4}$$

$$v_{xc}(\mathbf{r}) = \frac{\delta E_{xc}[n]}{\delta n(\mathbf{r})}, \tag{2.5}$$

$$n(\mathbf{r}) = \sum_{i\in occ} |\psi_i(\mathbf{r})|^2. \tag{2.6}$$

The success of this method relies in the good description of the kinetic and electrostatic terms and the appropriated description of the smaller exchange-correlation part, via a suitable mean-field approximation (valid in not too strongly-correlated materials).

The simplest approximation for the exchange-correlation energy is obtained taking $E_{xc}[n]$ to be a local functional of the density (Local Density Approximation or LDA) [23]:

$$E_{xc}^{LDA}[n(\mathbf{r})] = \int \epsilon_{xc}^{LDA}(n(\mathbf{r}))n(\mathbf{r})d\mathbf{r}, \tag{2.7}$$

where $\epsilon_{xc}^{LDA}(n)$ is the exchange-correlation energy density of a uniform electron gas with density n. The function $\epsilon_{xc}^{LDA}(n)$ has been calculated using Quantum Monte Carlo methods and then parametrized in a form suitable for practical calculations. The LDA approach has proved very useful approximation for a large class of materials. Typically LDA yields a good accuracy in the calculated structural and vibrational properties; it usually overestimates bonding energies and underestimates bond lengths, lattice spacings, and insulating band gaps.

2.2 Density functional perturbation theory

Once the unperturbed problem has been solved in DFT, DFPT provides an efficient method to calculate the electronic linear response to an external perturbation of arbitrary wavelength.

When an external perturbation λV_{bare} is superimposed to the external KS potential, the self consistent potential is modified accordingly:

$$V_{SCF} \rightarrow V_{SCF} + \lambda V_{SCF}^{(1)}, \tag{2.8}$$

where λ is the perturbation parameter, and the superscript $^{(1)}$ denotes the first order in λ variation of the ground state quantities.

From standard first order perturbation theory, the linear variation of a wavefunction $\psi_i^{(1)}$ and of the charge density $n^{(1)}$ can be obtained solving

self-consistently the following set of equations:

$$[H_{KS} + \alpha P_v - \epsilon_i] \left| P_c \psi_i^{(1)} \right\rangle = -P_c V_{SCF}^{(1)} |\psi_i\rangle \,, \tag{2.9}$$

$$n^{(1)}(\mathbf{r}) = 2\mathrm{Re} \sum_{i \in occ} \psi_i^\star(\mathbf{r}) \psi_i^{(1)}(\mathbf{r}), \tag{2.10}$$

$$V_{SCF}^{(1)}(\mathbf{r}) = V_{bare}(\mathbf{r}) + \int \frac{n^{(1)}(\mathbf{r}')}{|\mathbf{r} - \mathbf{r}'|} d\mathbf{r}' + n^{(1)}(\mathbf{r}) \left. \frac{dv_{xc}}{dn} \right|_{n=n_0} . \tag{2.11}$$

Here α is a parameter chosen is such a way that the left hand side operator is not singular; P_v and P_c are the projectors on filled (valence) and empty (conduction) states, respectively:

$$P_v = \sum_{i \in occ} |\psi_i\rangle \langle \psi_i| \,, \quad P_c = 1 - P_v. \tag{2.12}$$

The DFPT equations resemble very much the set of KS equations except that the first equation in the set is not an eigenvalue equation, but requires solving a linear problem. One of the main advantages of DFPT is that one can treat perturbations with arbitrary wavelength; different wavelengths are decoupled one from each other. This leads to an enormous time saving because calculations are done on the same small unit cell, independently of the wavevector of the perturbation.

2.3 Plane wave pseudopotential method

To solve numerically the KS equations it is necessary to expand the wavefunctions in a basis set. One of the most useful choices in ab-initio calculation for periodic systems, is that of plane waves (PW's)[1]:

$$\psi_{n\mathbf{k}} = e^{i\mathbf{k}\cdot\mathbf{r}} u_{n\mathbf{k}}(\mathbf{r}), \tag{2.13}$$

$$u_{n\mathbf{k}}(\mathbf{r}) = \sum_{\mathbf{G}} c_{n\mathbf{k}}(\mathbf{G}) e^{i\mathbf{G}\cdot\mathbf{r}}, \tag{2.14}$$

[1] *http://www.pwscf.org* describes the implementation we use here.

where n is the band index, $\mathbf{k}$ a point in the Brillouin zone, $u_{n\mathbf{k}}(\mathbf{r})$ is the periodic part of the Bloch wavefunction and $\mathbf{G}$ is a reciprocal lattice vector. The KS equation in reciprocal spaces becomes a linear problem:

$$\sum_{\mathbf{G}'} \left[\frac{1}{2}|\mathbf{k}+\mathbf{G}|^2\delta_{\mathbf{G},\mathbf{G}'} + V_{SCF}(\mathbf{G}-\mathbf{G}')\right] c_{n\mathbf{k}}(\mathbf{G}') = \epsilon_{n\mathbf{k}} c_{n\mathbf{k}}(\mathbf{G}). \tag{2.15}$$

The size and accuracy of the calculation is set by fixing the kinetic energy cutoff for the truncation of the basis:

$$\frac{1}{2}|\mathbf{k}+\mathbf{G}|^2 < E_{cut}. \tag{2.16}$$

The main advantage of the PW basis set lies in its translational invariance properties, in the existence of a simple parameter controlling the accuracy and in the availability of Fast Fourier Transform. However, on the other hand, this choice of basis implies the same resolution in every region of space so that it is impossible to describe, with a manageable number of PW's, the oscillations of the wavefunction of core electrons. That requires the use of pseudopotentials which are built to describe in an effective way the interaction between core and valence electrons, considering core electrons as frozen. Pseudopotentials are required to reproduce – at the reference electronic configuration – both the energies and the wavefunctions of the all-electron valence states outside the core region.

This approach makes it possible to perform the calculations with a manageable energy cutoff for the PW basis set. Details about the pseudopotentials used in this work will be given in the following chapters.

2.4 Linear response to a uniform magnetic field

The external applied magnetic field enters the electronic hamiltonian in the kinetic energy term, via minimal coupling $p \to (p - eA/c)$ with the vector potential A, the field being $\mathbf{B} = \nabla \times \mathbf{A}$. Treating the magnetic field magnitude B as a small perturbation, we expand the kinetic energy in powers of

A, and retain only the first order "paramagnetic" terms:

$$\frac{1}{2m}\left[\mathbf{p}+\frac{e}{c}\mathbf{A}(\mathbf{r})\right]^2=\frac{\mathbf{p}^2}{2m}+\frac{e}{2mc}\left(\mathbf{p}\cdot\mathbf{A}+\mathbf{A}\cdot\mathbf{p}\right)+\frac{1}{2mc^2}\left|\mathbf{A}(\mathbf{r})\right|^2, \quad (2.17)$$

and neglecting the last (diamagnetic) term.

In isolated systems (atoms, molecules) one can safely choose a gauge in which the vector potential is proportional to the coordinate **r** (i.e. the Landau or symmetric gauge $\mathbf{A} = (1/2)\mathbf{B}\times\mathbf{r}$), but this choice is problematic in a periodic system. One possible solution was adopted by Sebastiani and Parrinello [24]. They transform the homogeneous magnetic field into a periodic one, by defining a new periodic position operator **r** [25]. This is done by a unitary transformation from the subspace of the occupied wavefunctions, maximally localized Wannier functions [26]. The unit cell is chosen large enough so that each Wannier function is significantly different from zero only within a limited region of the unit cell. The position operator, when acting on a Wannier function, can be replaced a saw-tooth shape whose discontinuities fall in regions of space where the wavefunction is close to zero.

A different approach introduced by Mauri and collaborators [27, 28, 29, 30, 31], is based on the substitution of the homogeneous magnetic field, with a long wavelength modulated magnetic field $B = B_0\exp(i\mathbf{q}\cdot\mathbf{r})$. In this approach the vector potential is chosen as:

$$\mathbf{A}(\mathbf{r}) = iB\frac{\mathbf{q}\times\hat{b}_q}{|q|^2}\exp(i\mathbf{q}\cdot\mathbf{r}). \quad (2.18)$$

By taking the curl of **A**, the magnetic field is:

$$\mathbf{B} = B\,\hat{b}_q\exp(i\mathbf{q}\cdot\mathbf{r}), \quad (2.19)$$

where: $\hat{b}_q$ and B are the direction and the intensity of the magnetic field and **q** is a wavevector with $|q|\ll 1$ and $\mathbf{q}\perp\hat{b}_q$.

The action of the first order perturbation operator on a Bloch wavefunction is:

$$\mathcal{H}_1 = \frac{e}{2mc}\left(\mathbf{p}\cdot\mathbf{A}+\mathbf{A}\cdot\mathbf{p}\right), \quad (2.20)$$

$$\left\langle \mathbf{r} \left| \mathcal{H}_1 \right| e^{i\mathbf{kr}} u_k(\mathbf{r}) \right\rangle = -\frac{e^{i(\mathbf{k}+\mathbf{q})\cdot\mathbf{r}}}{m} \left(\frac{B}{c}\right) \frac{\mathbf{q}\times\hat{b}_q}{|q|^2} \left[\vec{\nabla} + i\left(\mathbf{k}+\frac{\mathbf{q}}{2}\right) u_k(\mathbf{r})\right], \quad (2.21)$$

$$\left\langle u^{(j)}_{k+q} \left| \mathcal{H}_1 \right| u^{(i)}_k \right\rangle = \sum_{\mathbf{G}} c^{(j)*}_{G,k+q} c^{(i)}_{G,k} \left[-\frac{iB}{mc}\left(\frac{\mathbf{q}\times\hat{b}_q}{|q|^2}\right)\cdot\left(\mathbf{k}+\mathbf{G}+\frac{\mathbf{q}}{2}\right)\right]. \quad (2.22)$$

This relation can be implemented very quickly in the existing linear response plane wave code. As pointed out by Mauri and coworkers [32], the operator $(-i\nabla + \mathbf{k} + \mathbf{q}/2)$ can, in pseudopotential calculations, be replaced by the velocity operator $\mathbf{v}_{\mathbf{k},\mathbf{k}'} = -i\nabla + \mathbf{k}' - i\left[\mathbf{r}, V^{nl}_{\mathbf{k},\mathbf{k}'}\right]$ where $V^{nl}_{\mathbf{k},\mathbf{k}'}$ is the non-local pseudopotential operator.

We choose Mauri and coworkers method because it can be implemented quickly and accurately within our existing linear response code. The actual calculations are done in three steps:

1. A standard SCF electronic structure calculation is done, in order to get the self consistent potential and the ground state wavefunctions $u^{(i)}_k$.

2. A non-SCF calculation is done, by using the self consistent potential calculated at the previous step; the hamiltonian is diagonalized at each $\mathbf{k}+\mathbf{q}$ point yielding the $u^{(i)}_{k+q}$ functions.

3. Finally a linear perturbation calculation is done, giving the perturbed wavefunctions $\Delta u^{(i)}_{k,q}$.

2.5 Adiabatic approximation in a magnetic field

If the standard Born-Oppenheimer factorization of a molecular wavefunction into a product of electronic and nuclear parts is applied to a molecular system in an external magnetic field, the resulting effective Hamiltonian for the nuclear motion is that of "bare" nuclear charges interacting with the magnetic field. The reason for this is that the Born-Oppenheimer procedure calls for the averaging of electronic properties for fixed nuclei before considering the

nuclear motion. Thus, any effect of the velocity acquired by the electrons as they "follow" the nuclear motion is lost, and this of course includes the force experienced by electrons as well as nuclei as the molecular system moves in an external magnetic field [17].

Since the application of this "naive" Born-Oppenheimer procedure is evidently wrong as it would predict that a neutral atom would be deflected in a magnetic field as if it were a bare nucleus, it follows that some modification of the procedure is called for in the presence of a magnetic field.

The Born-Oppenheimer approximation starts by writing the total (nuclear and electronic) wavefunction as a the product:

$$\Psi(\mathbf{r}, \mathbf{R}) = \psi_{nu}(\mathbf{R})\psi_{el}(\mathbf{r}; \mathbf{R}). \tag{2.23}$$

The aim is to obtain an effective Schrödinger equation for the nuclear wavefunction ψ_{nu} where the electronic degrees of freedom have been integrated out. We start by considering the effect of the canonical nuclear momentum $\hat{\mathbf{P}}$ on the total wavefunction:

$$\hat{\mathbf{P}}\Psi(\mathbf{r}, \mathbf{R}) = -i\hbar\ \psi_{el}(\mathbf{r}; \mathbf{R})\nabla_{\mathbf{R}}\psi_{nu}(\mathbf{R}) - i\hbar\ \psi_{nu}(\mathbf{R})\nabla_{\mathbf{R}}\psi_{el}(\mathbf{r}; \mathbf{R}). \tag{2.24}$$

Then, multiplying to the left with ψ_{el} and integrating over the electronic degrees of freedom, we get the effective nuclear momentum acting on $\psi_{nu}(\mathbf{R})$:

$$\hat{\mathbf{P}}\psi_{nu}(\mathbf{R}) = -i\hbar\ \nabla_{\mathbf{R}}\psi_{nu}(\mathbf{R}) - i\hbar\ \langle\psi_{el,\mathbf{R}}|\nabla_{\mathbf{R}}|\psi_{el,\mathbf{R}}\rangle\ . \tag{2.25}$$

The last term appearing in eq. 2.25 is called "geometric vector potential" (GVP) or "Berry connection", as it has the same properties of a vector potential [15]. The rest of this review part follows that given by Resta [18].

Whenever the electronic wavefunction can be chosen as real (i.e. without any external magnetic field and if there is no degeneracy), the GVP vanishes and the kinematic momentum $\hat{\mathbf{P}}$ is equal to the canonic one ($-i\hbar\nabla_{\mathbf{R}}$). But if we follow the adiabatic evolution of the electronic wavefunction along a closed path in $\{\mathbf{R}\}$ space encircling a degeneracy, then the electronic wavefunction can undergo a sign change. As the total wavefunction must be single-valued,

also the ionic wavefunction must undergo a sign change, a Berry phase [15]. This sign change is a boundary condition which modifies the spectrum of the effective nuclear hamiltonian and which has in fact remarkable observable effects on the rotovibrational spectrum of some molecules [33, 34, 35].

If on the other hand, even in absence of level crossing, but when a genuine magnetic field is applied, the electronic wavefunction is necessarily complex and the GVP doesn't vanish. Now the nuclear equation of motion includes two vector potentials and if we treat this equation of motion at a classical level, there will be two "Lorentz forces". The curl of the vector potential is of course the physical magnetic field, while the curl of the GVP is a "magnetic-like" field which, in general, does not vanish. It has to be stressed here that the true, physical magnetic field present is that arising from the vector potential; for instance, in an NMR experiment, the nuclear spins see the external magnetic field plus the induced magnetic field generated by the surrounding electrons. The additional "magnetic-like" field affects only the mechanical, or "orbital" nuclear motion.

Within a naive Born-Oppenheimer approximation – i.e. neglecting this extra geometric vector potential – the physical magnetic field acts on the nuclei as if they were "naked" charges; it is pretty clear however that the GVP term is no small correction. This is easily illustrated in the simple case of a neutral hydrogen atom moving at constant speed in a uniform magnetic field.

2.6 An illuminating example: hydrogen atom in a magnetic field

Suppose we take a neutral hydrogen atom in a uniform magnetic field; then the full hamiltonian, neglecting the Zeeman effect becomes:

$$\mathcal{H} = \frac{1}{2M}\left[\mathbf{P} + \frac{e}{c}\mathbf{A}(\mathbf{R})\right]^2 + \frac{1}{2m}\left[\mathbf{p} - \frac{e}{c}\mathbf{A}(\mathbf{r})\right]^2 - \frac{e^2}{|\mathbf{R}-\mathbf{r}|}, \tag{2.26}$$

where we took e, the electron charge, negative. Now in the screened Born-Oppenheimer approximation the correct hamiltonian is:

$$\mathcal{H} = \frac{1}{2M}\left[\mathbf{P} + \frac{e}{c}\mathbf{A}(\mathbf{R}) - \chi(\mathbf{R})\right]^2 + E(\mathbf{R}), \tag{2.27}$$

where $E(\mathbf{R})$ is the ground state energy of the electronic problem in presence of the magnetic field:

$$h_{\mathbf{R}}(\mathbf{r}) = \frac{1}{2m}\left[\mathbf{p} - \frac{e}{c}\mathbf{A}(\mathbf{r})\right]^2 - \frac{e^2}{|\mathbf{R}-\mathbf{r}|}, \tag{2.28}$$

and $\chi(\mathbf{R})$ is the geometric vector potential, given by:

$$\chi(\mathbf{R}) = i\langle\psi_{\mathbf{R}}(\mathbf{r})|\nabla_{\mathbf{R}}\psi_{\mathbf{R}}(\mathbf{r})\rangle, \tag{2.29}$$

where $\psi_{\mathbf{R}}(\mathbf{r})$ is the ground state of $h_{\mathbf{R}}(\mathbf{r})$.

For the free motion of the H atom, the exact form of the wavefunction $\psi_{\mathbf{R}}(\mathbf{r})$ is known by gauge-invariance to be of the form:

$$\psi_{\mathbf{R}}(\mathbf{r}) = \exp\left[\frac{ie}{2c}\mathbf{r}\cdot\mathbf{B}\times\mathbf{R}\right]\psi_0(\mathbf{r}-\mathbf{R}), \tag{2.30}$$

where $\psi_0(\mathbf{r})$ is the electronic ground state wavefunction when the proton is at $\mathbf{R} = 0$ and the phase factor is just that needed to translate from the gauge $\mathbf{A} = \frac{1}{2}\mathbf{B}\times\mathbf{r}$ to the gauge $\mathbf{A} = \frac{1}{2}\mathbf{B}\times(\mathbf{r}+\mathbf{R})$ (both describing the same field $\mathbf{B}$). The Berry connection is:

$$\begin{aligned}\chi(\mathbf{R}) &= \frac{e}{2c}\langle\psi_0(\mathbf{r}-\mathbf{R})|\mathbf{B}\times\mathbf{r}|\psi_0(\mathbf{r}-\mathbf{R})\rangle + \\ &+ i\langle\psi_0(\mathbf{r})|\nabla_{\mathbf{R}}\psi_0(\mathbf{r})\rangle = \\ &= \frac{e}{2c}\mathbf{B}\times\mathbf{R} = \frac{e}{c}\mathbf{A}(\mathbf{R}),\end{aligned} \tag{2.31}$$

which cancels exactly the term giving the Lorentz force on the bare nuclear charge.

2.7 Integral formulation and Berry phase

The previous calculation is a particular case where the Berry connection can be evaluated in a trivial manner. In a general case, the evaluation of the

Berry connection is not an easy task, as explained in the previous section. The problem is that the GVP is not gauge-invariant; we need to restate the problem in a gauge-invariant way, since only gauge-invariant quantities have a physical meaning.

The solution is to carry out a contour integral of the GVP around a close loop in configuration space; the resulting quantity is called Berry phase (γ). It can be proved that the Berry phase is gauge invariant, and therefore it can be a physical observable [15, 18]:

$$\gamma = i \oint \chi(\mathbf{R}) \cdot d\mathbf{R}. \tag{2.32}$$

Indeed, many manifestations of Berry phase do exist, and have been subject by several studies. Well known solid state applications include the Aharonov-Bohm effect, the macroscopic polarization in insulators [36], spin-wave dynamics [37]. Here, we will show that for rotating molecules, the Berry phase influences the rotational g-factor, a term which accounts for the screening of rotational magnetic moment of the nuclei, by the electrons.

In order to calculate this magnetic screening, we integrate also the classical vector potential term (which of course depend on the choice of the gauge) around the same closed path, getting the magnetic flux through the surface embraced by the circuit:

$$\Phi = \frac{e}{c} \oint_{\partial S} \mathbf{A}(\mathbf{R}) \cdot d\mathbf{R} = \frac{e}{c} \iint_S \mathbf{B} \cdot d\mathbf{S}. \tag{2.33}$$

If the electrons were absent, Φ would be the phase factor acquired by the nuclear wavefunction after a closed loop. The electrons contribute with the additional Berry phase γ, that can compensate, or even overcome, the nuclear contribution. The compound result is that the nuclear wavefunction acquires a phase factor as if the magnetic field were replaced by an effective magnetic field:

$$B_{\text{eff}} = (1 + \sigma)B, \quad \sigma = \gamma/\Phi, \tag{2.34}$$

where we have defined σ as the "magnetic screening". In our convention, the Berry phase γ and the bare magnetic phase Φ generally have opposite signs; hence σ is negative.

In order to carry out numerically the integral 2.32, it is substituted by a finite summation over a discrete set of points along the path (fig. 2.1). It has been shown by Resta [18] that for a system of non interacting electrons (i.e. the wavefunction is a single Slater determinant), the Berry phase is given by:

$$\gamma \simeq -\mathrm{Im}\log \prod_{\xi=0}^{N-1} \det \mathcal{S}(\xi, \xi+1), \tag{2.35}$$

where the matrix elements of $\mathcal{S}$ are the overlap between occupied single-particle wavefunctions at consecutive ξ points along the integration path:

$$\mathcal{S}_{ij}(\xi, \xi+1) = \langle \psi_i(\xi) | \psi_j(\xi+1) \rangle \,. \tag{2.36}$$

These expression can be implemented straightforwardly in an existing electronic structure code.

The integral formulation of the Berry phase has several advantages relative to the differential formulation, involving the GVP. For a complex hamiltonian (the way our code is implemented generally yields complex wavefunctions and hamiltonians even in zero field), if the state $|\psi(\xi)\rangle$ is obtained by numerical diagonalization, the phase at each ξ-point is chosen at random by the diagonalization routines and shows no regularity at all when the set becomes denser and denser. Notwithstanding this, the discrete expression for the Berry phase does converge to a meaningful value. Also, if the occupied orbitals are degenerate at some ξ-point, there is an ambiguity in defining the ξ-dependence of each orbital separately. This causes no problems in the discrete formulation for the Berry phase, a quantity uniquely determined by the condition that the highest occupied orbital be separated by a finite gap from the lowest unoccupied at any ξ-point of the path (level crossings can only come in pairs leading at most to a Berry phase of π).

In the present case, we calculate the Berry phase of the full electronic wavefunctions, perturbed to linear order by the magnetic field:

$$\psi_i(\xi) = \psi_i^{(0)}(\xi) + \frac{B}{c}\psi_i^{(1)}(\xi), \tag{2.37}$$

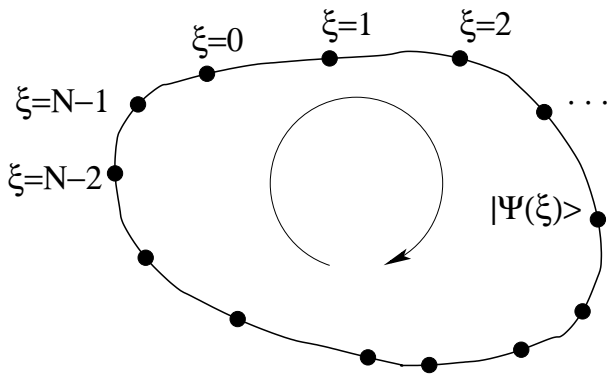

Figure 2.1: Adiabatic evolution of a ket $|\psi(\xi)\rangle$ along a discretized closed path in parameters space.

where $\psi_i^{(0)}(\xi)$ is the unperturbed wavefunction for a given ξ point, and $\psi_i^{(1)}(\xi)$ is the linear term in the perturbation of $\psi_i^{(0)}(\xi)$ by the magnetic field. Equation 2.36 becomes:

$$S_{i,j}(\xi, \xi+1) = \left\langle \psi_i^{(0)}(\xi) + \frac{B}{c}\psi_i^{(1)}(\xi) \middle| \psi_i^{(0)}(\xi+1) + \frac{B}{c}\psi_i^{(1)}(\xi+1) \right\rangle. \quad (2.38)$$

In the previous equation we retained only the terms up to first order in the magnetic field, and discarded the quadratic term $(B/c)^2 \left\langle \psi_i^{(1)}(\xi) \middle| \psi_i^{(1)}(\xi+1) \right\rangle$. The resulting Berry phase γ is proportional to (B/c).

The flux Φ of the magnetic field (eq. 2.33) can be calculated straightforwardly and in practical calculation, we set the perturbation parameter (B/c) to a small value (10^{-6}).

Chapter 3

Rotational g-factor in molecules

In the previous chapter we showed how the geometric vector potential (GVP) can account from the screening of the bare nuclear Lorentz force by the electrons for a neutral atom in a magnetic field. The proof can be easily generalized to any neutral molecule with all nuclear degrees of freedom "frozen" except for the center of mass translation.

In this chapter, we consider a molecular system in which all nuclear degrees of freedom are frozen except rotation about the center of mass. In case of a rotation in a uniform field, the question of the electronic contribution to the interaction of the molecule with the field may be restated as that of the electronic contribution to the orbital magnetic moment. That contribution "screens" that of the bare nuclei giving rise to a rotational g-factor ranging from one (no screening), to zero (perfect screening) and to negative values (over-screening).

3.1 Rotational g-factor

Let's consider a rigid nuclear framework rotating at constant speed ω around a fixed axis. The rotational g-factor tensor is defined as minus the second derivative of the energy respect to the magnetic field $\mathbf{B}$ and to the angular

momentum **L**:

$$\mathcal{H}_{Zeeman} = -g\mu_N \mathbf{L} \cdot \mathbf{B}, \tag{3.1}$$

$$g_{ij} = -\frac{1}{\mu_N} \frac{\partial^2 E}{\partial L_i \partial B_j}, \tag{3.2}$$

where μ_N is the nuclear magneton, equal to $e/(2m_p c)$, where m_p is the proton mass.

From equation 3.1, it can be recognized that the magnetic moment μ is equal $g\mu_N \mathbf{L}$; so that, the g-factor can be expressed as the ratio between the magnetic moment μ and the angular momentum **L**, in units of the nuclear magneton:

$$g = \frac{1}{\mu_N} \frac{\mu_{nu} + \mu_{el}}{L}. \tag{3.3}$$

The electrons contribute only the orbital magnetic moment, as in a closed shell molecule, the sum of the angular momentum of all the electrons is zero. Treating the nuclei from a classical point of view:

$$\mu_{nu} = |e| \sum_i (Z_i/c)\ \pi r_i^2\ \nu, \tag{3.4}$$

$$L = I\omega = \sum_i M_i\ 2\pi\nu\ r_i^2, \tag{3.5}$$

where the sum runs on the nuclei, Z_i and M_i are the charge and mass of the nucleus i, r_i is distance of the nucleus from the rotation axis and ν is the frequency of rotation.

The "magnetic screening", defined as the ratio between the electronic magnetic moment and the rotational nuclear one, is:

$$\sigma = \frac{\mu_{el}}{\mu_{nu}} = -1 + g\frac{\sum_i m_i r_i^2}{\sum_i Z_i r_i^2} \quad \text{(generally} < 0), \tag{3.6}$$

where $m_i = M_i/m_p$ is the nucleus mass in unit of the proton mass. Inverting this relation, we finally obtain the expression of the rotational g-factor in terms of the magnetic screening:

$$g = (\sigma + 1)\frac{\sum_i Z_i r_i^2}{\sum_i m_i r_i^2}. \tag{3.7}$$

From this expression, the qualitative significance of the rotational g-factor becomes immediately clear:

- a g-factor close to one means that the σ is close to zero, and that the electrons screen poorly the nuclei;
- a g-factor close to zero, on the contrary, means that the electrons screen almost completely the nuclear charges;
- a negative g-factor means that $\sigma < -1$ and that the electrons give rise to a magnetic moment contrary and greater than that of the bare charges of the nuclei (overscreening); the total magnetic moment is opposite in direction with respect to the rotational angular momentum.

The test molecules we have investigated (hydrogen molecular ion H_2^+, hydrogen H_2, acetylene C_2H_2, methane CH_4 and fluoromethane CF_4) exhibit the full range of g-factors.

As shown in ref. [14], the electronic contribution to the rotational g-factor is related to the paramagnetic part of the susceptibility tensor χ^p:

$$g^{el}_{\alpha\beta} = g^{\text{bare}} \frac{\sigma}{1+\sigma} = -4M_p \frac{\chi^p_{\alpha\beta}}{I_\alpha}, \tag{3.8}$$

where g^{bare} is the g-factor as if the nuclei where naked, M_p is the proton mass and I_α is the α component of the moment of inertia. The magnetic field perturbs the electronic structure of the molecule, inducing paramagnetic and diamagnetic currents (e.g. ring currents in aromatic compounds like benzene). The induced currents generate a field-induced magnetic moment, equal to the the paramagnetic susceptibility times the magnetic field.

Thus, poor magnetic screening corresponds to small paramagentic susceptibility; conversely, almost complete screening, corresponds to large paramagnetic susceptibility.

3.2 Details of practical calculations

In order to calculate the magnetic screening, we applied the procedure illustrated at end of the previous chapter. The Berry phase was calculated

using the discrete formulation (eq. 2.35). The ξ points in nuclear configuration space correspond, in the simple case of rotation, to the perfect circular trajectories covered by the nuclei, rotating around the center of mass of the molecule.

The practical computation consists in a sequence of calculations for many rotated configuration of the molecule. The rotated configuration does not span the full circumference, but only a symmetry-irreducible interval. For instance, in the case of linear molecules, it is sufficient to span the $[0, \pi)$ interval. For CH_4 and CF_4 it is sufficient to span the $[0, 2\pi/3)$ interval. The angle increment was 6° ($\pi/30$).

Molecules were placed in a periodically repeated cubic cell with enough empty space in order to minimize interactions between them. For practical calculations we set $|q| = 0.01(2\pi/a)$ where a is the side of the cubic cell.

As explained in the previous chapter, we performed three calculations for each configuration: a standard SCF calculation; a non-SCF calculation of the wavefunctions at $\mathbf{q}$; a linear response calculation giving the pertubed wavefunctions. The nuclear contribution to the orbital magnetic moment is calculated straighforwarldy, given the geometry of the molecule.

3.3 Hydrogen molecular ion H_2^+

As the first test case we studied the rotation of the simplest molecule, namely the hydrogen molecular ion H_2^+. This is a single electron molecule, whose Schrödinger equation for fixed nuclear separation can be solved exactly and analytically [38]. The exact solution gives an equilibrium separation between the nuclei of 2.0 a.u.; the ground state wavefunction shows two cusps in correspondence of the nuclei.

We set the bond distance at the equilibrium value of 2.0 a.u. and used for the electron-proton interaction the bare coulomb potential. In order to make use of our cell-periodic plane-wave scheme of chapter 2, the molecule was placed in a cubic cell with lattice spacing set to 6 Å. The magnetic

field was placed orthogonal to axis of the molecule. As the energy cutoff required for solving exactly the full potential problem should be infinite, we increased the cutoff of the plane wave expansion from 80 Ry to 200 Ry, in order to estimate the convergence of the g-factor. The results, given in table 3.1, show that 80 Ry is already accurate to within $2{\cdot}10^{-4}$ accuracy. We obtained an exact electron screening of -5.43%, corresponding to a g-factor of 0.946 in H_2^+. This, we note, is a very poor screening, reflecting the effective concentration of the electron magnetic response in the vicinity of the bond center. Note that there is no such concentration in the charge density, which has instead a minimum at the bond center. Magnetic screening is therefore a very independent quantity with respect to the electron charge distribution. By comparison, the rotational g-factor generated by e.g. rigidly rotating the static electronic charge of H_2^+ is calculated to be -0.83, a very different value. The reason for this is that the charge density of H_2^+ extends in a region of space far away from the nuclei and the expectation value of (x^2+y^2) is larger than the square of the proton-proton distance R^2 (fig. 3.1).

Lacking an experimental comparison, our accurate result $g = 0.946$, while confirming an earlier variational estimate of about -5% [39], can be used to test the standard self-consistent (SCF) pseudopotential electronic structure calculations to be routinely used later on.

Carrying out again the calculation for H_2^+, but using now a pseudopotential for H, and standard self-consistency as if H_2^+ were a many-electron system (we used non spin-polarized LDA functional with the orbital occupation equal to one) we found a magnetic screening of -5.75%, corresponding to a g-factor of 0.9425, in close agreement with the exact result 0.946.

Satisfied by this check we can move on to calculate the rotational g-factor of the hydrogen molecule (H_2) and other molecules.

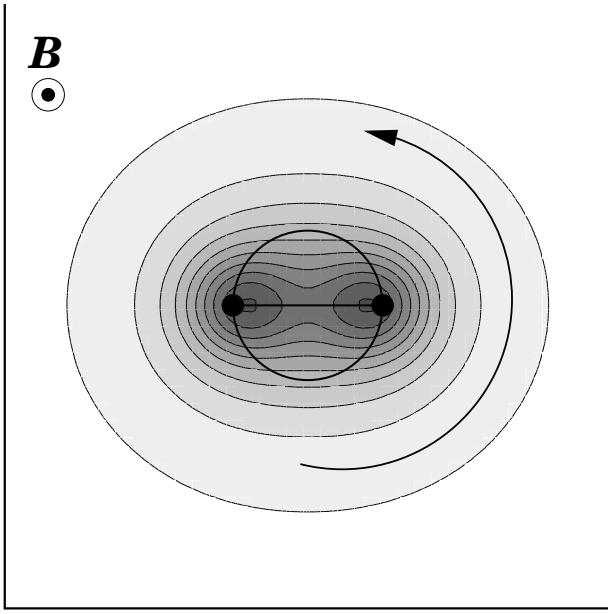

Figure 3.1: H_2^+ charge density plot. The protons are indicated by the full circles and rotates on a circular trajectory. The magnetic field is perpendicular to the plane of the figure.

screening	**g-factor**	**notes**
H_2^+ rotation:		
-5.41%	0.9459	EX, 80 Ry
-5.42%	0.9458	EX, 120 Ry
-5.43%	0.9457	EX, 160 Ry
-5.43%	0.9457	EX, 200 Ry
-5.75%	0.9425	SCF, pseudopot., 80 Ry

Table 3.1: Plane wave results for the rotational g-factor of the hydrogen molecular ion H_2^+; EX stands for "exact" calculation, i.e. one electron full potential; SCF stands for self-consistent calculation with a pseudopotential for hydrogen.

3.4 Hydrogen and other molecules

Using the experimental bond length of 1.4 a.u. for H_2, we performed a SCF calculation with a plane wave cutoff of 80 Ry and obtained a magnetic screening of -12.45%, corresponding to a g-factor of 0.8755. That is in excellent agreement with the experimental value of 0.8787 obtained long ago by Ramsey [2]. Comparison with H_2^+ indicates that the two electrons of H_2 just approximately double to -12.45% the single electron screening -5.4% of H_2^+, irrespective of a factor 1.42 in the H–H distance.

In order to further benchmark the accuracy of our method, we considered next molecules with larger magnetic screening and smaller g-factors [3], namely the linear acetylene (C_2H_2), and the tetrahedral methane (CH_4) and carbon tetrafluoride (CF_4) molecules. In these molecules the C–H and C–F bonds possess a partly ionic character, some electron fraction attracted to a larger distance from the center, and thus likely to screen more effectively the nuclei.

In all three cases, we used the experimental bond-lengths and a plane wave cutoff of 80 Ry. The three molecules were placed in repeated cubic cell with a lattice spacing of 9 Å; the magnetic field was placed parallel to the principal rotation axis of the molecule, i.e. perpendicular to the molecule for C_2H_2 and parallel to a bond for CH_4 and CF_4.

Our results (table 3.2) confirm a large screening value and (except for CH_4) agree very closely with experiment where available. The small g-factor value is thus an indicator of ionicity, whereas (as exemplified by H_2) a g-factor close to 1 is characteristic of the covalent bond.

The marginally positive g-factor of C_2H_2 confirms the nearly perfect screening of nuclei, whereas the marginally negative g-factor of CF_4 indicates a slight overscreening ($|\sigma| > 1$), probably due to an important electron fraction that effectively orbits beyond the C-F distance. In fact, inverting equation 3.7, one gets $Z_i = 7.658$ electrons for the fluorine atom (7.462 from the experimental g-factor), with about half an electron beyond neutrality. For CH_4, our calculated rotational g-factor (0.20) compares less favorably with

the experimental value of 0.313 and the most accurate quantum chemistry value of 0.319 [40]. The reason for this unexpected discrepancy is unclear and is being presently pursued.

The g-factor can be revealed experimentally also as a field-induced splitting of the rotational states of two coupled rotating methyl groups. In fact Peternelj and coworkers [41], by NMR spectroscopy studied the constrained rotations of methyl end groups ($-CH_3$) about C-C bond in amorphous organic samples [41]. In particular for the $L = 1$ rotational state, the frequency shift is given by:

$$\Delta E = \mu_N \; g \; B = 7.622 \text{ MHz } g \; \frac{B}{\text{Tesla}}, \tag{3.9}$$

where B is in Tesla; the numeric coeffiecient 7.622 MHz corresponds to the splitting of the rotational state for a field of 1 Tesla and g=1. Measurements in acetyl-acetone ($CH_3CO-COCH_3$) show a splitting of about 38 kHz for a field of 0.05 Tesla, corresponding to a methyl group g-factor of about 0.1. Thus screening is somewhat larger than that for single CH_4 molecule (g =0.3), most likely reflecting a slight increase in ionicity of the methyl C–H bonds, compensating the decrease in the C–C bond. This underlines an exquisite sensitivity of the rotational g-factor to even delicate changes of the chemical circumstances.

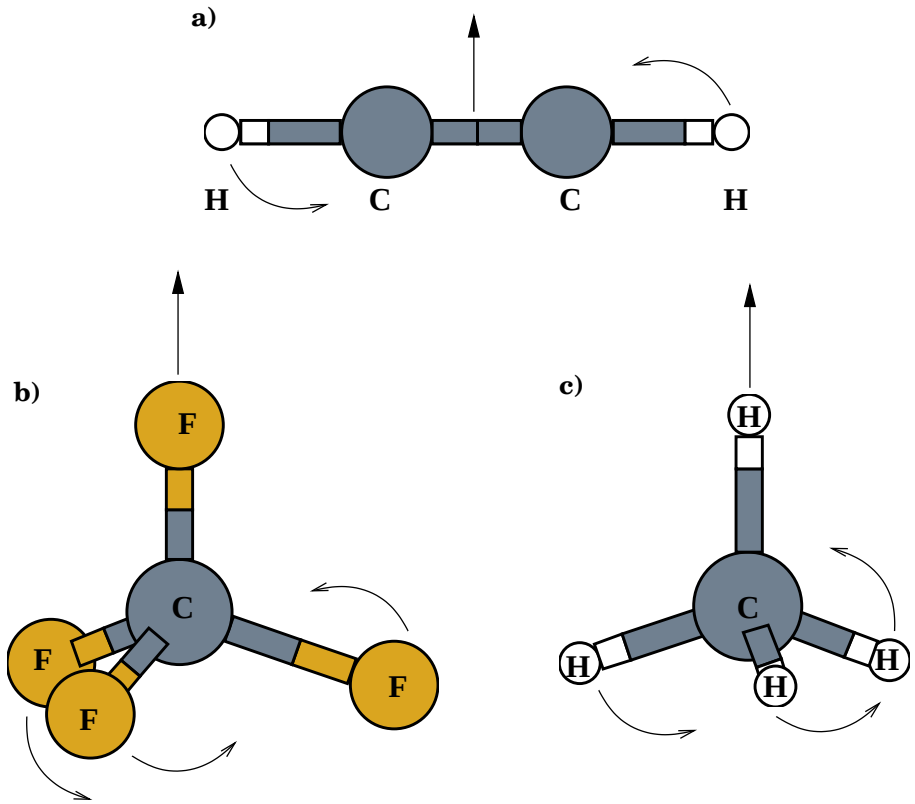

Figure 3.2: Structure of the three molecules under study. The arrows indicate the rotation axis and the magnetic field. a) acetylene H–C≡C–H. b) Fluoromethane CF_4. c) Methane CH_4.

screening	**g-factor**	**notes**
H_2 rotation:		
-12.45%	0.8755	
-12.13%	0.8787	Expt. [2]
-11.01%	0.8899	From MC-SCF theory [40]
C_2H_2 rotation:		
-94.2%	0.0405	
-92.9%	0.0490	Expt. [3]
-91.7%	0.0570	From MC-SCF theory [40]
CF_4 rotation:		
-109.4%	-0.0445	
-106.6%	-0.0312	Expt. [3]
CH_4 rotation:		
-79.6%	0.2047	
-68.7%	0.3133	Expt. [1]
-68.1%	0.3190	From MC-SCF theory [40]

Table 3.2: Plane wave results for the rotational g-factor of some molecules, compared to existing experimental data (Expt.) and to previous quantum chemical results [40].

3.5 Pseudorotations

In the chemical literature [42], a pseudorotation is defined as a cyclic motion of the atoms resulting in a structure that appears to have been produced by rotation of the entire initial molecule and is superposable on the initial one, unless different positions are distinguished (e.g. by isotopic substitution of the atoms).

Pseudorotations appear in molecules and in solids also as suitably degenerate vibrational modes and are generated by a linear combination of degenerate vibrational modes. Like genuine rotations, an angular variable can be associated with the pseudorotation (θ for a twofold degenerate state, (θ, ϕ) for a threefold degenerate state).

For a twofold degenerate vibrational mode, the linear combination of the two vibrational mode with a phase angle θ:

$$\mathbf{u}_{i,\alpha} = \left[\mathbf{u}^{(1)}_{i,\alpha} \cos\theta + \mathbf{u}^{(2)}_{i,\alpha} \sin\theta\right] \quad \alpha = x, y, z, \tag{3.10}$$

generates a pseudorotation, where the nuclei cover small orbits around a high symmetry configuration.

A simple example of pseudorotation is shown in fig. 3.3 for an equilateral triangle-shaped A_3 molecule. This molecule have a non-degenerate vibration A_1 mode and a twofold degenerate E_1 mode. Combining the two E_1 eignemodes, when θ ranges from 0 to 2π, the atoms follow a continue circular path around the high symmetry configuration and the molecule "appears" to rotate, hence the name pseudorotation (fig. 3.4).

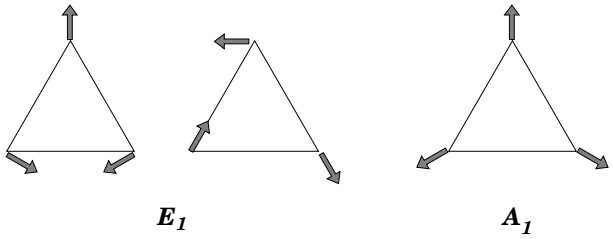

Figure 3.3: Vibrational modes of an equilateral triangle-shaped molecule. The E_1 modes are degenerate.

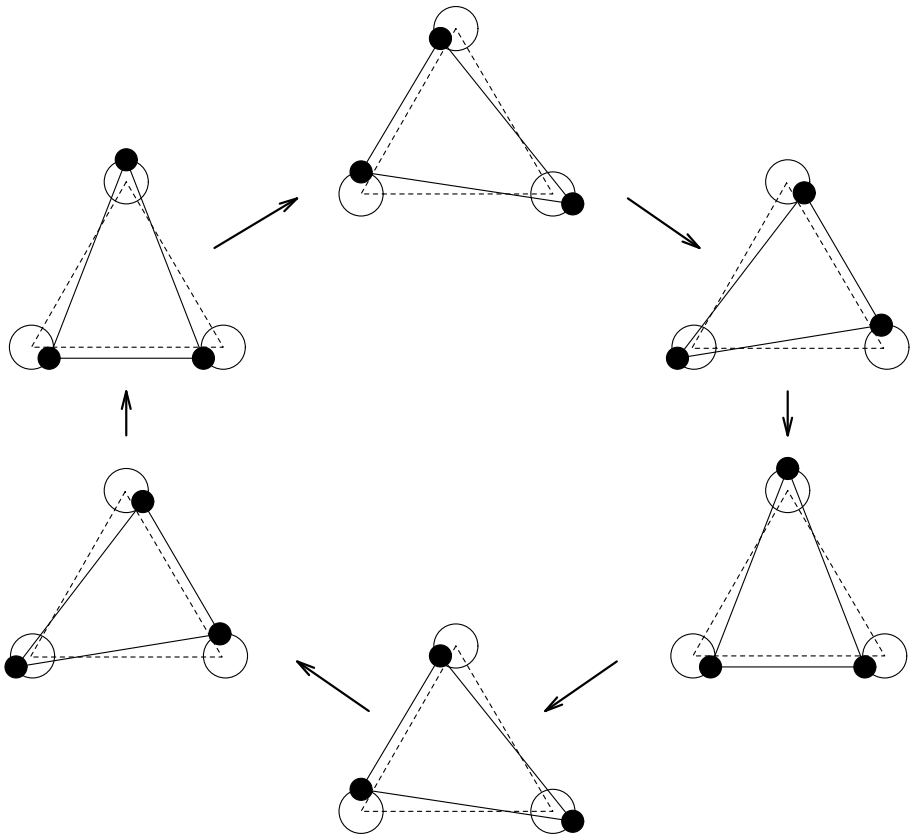

Figure 3.4: Pseudorotation generated by the E_1 eigenmodes of an equilateral triangle-shaped molecule (from [43]).

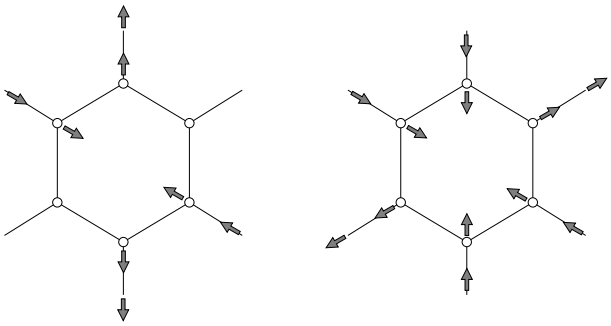

Figure 3.5: Schematic representation of two degenerate eigenvector of the ν_{18} mode in benzene, following Herzberg [44].

3.6 Pseudorotation in benzene

Besides rotations, the present technique can be directly applied to calculate g-factors for pseudorotations. As a simple prototype, we chose the lowest E_2 mode of benzene C_6H_6, of frequency ν_{18} at 606 cm^{-1} [44]. The eigenmodes of the lowest frequency E_1 mode are perpendicular to the benzene ring and does not encircle any area. Here instead, the nuclei move in the molecular plane, and the pseudorotation is generated by combining the two eigenmodes (fig. 3.5) with a phase factor:

$$\mathbf{u}_{i,\alpha} = A(\theta)\left[\mathbf{u}^{(1)}_{i,\alpha}\cos\theta + \mathbf{u}^{(2)}_{i,\alpha}\sin\theta\right]. \tag{3.11}$$

where $A(\theta)$ is the amplitude, i runs over the atoms and $\alpha = x, y, z$.

For a general large distortion, $A(\theta)$ should of course be determined for each angle θ , giving a generally non-circular pseudorotation orbit.

From a classical point of view, the amplitude $A(\theta)$ of the oscillation of a harmonic oscillator is given by the points of inversion of the motion. They are fixed by the inital conditions (initial elongation, or equilvalently total energy) and they can assume any value.

For the quantum harmonic oscillator, energy is quantized and only the expectation value of the amplitude $\sqrt{\langle x^2\rangle}$ can be calculated. Moreover, for

g-factor	**amplitude** $A(\theta)$
0.7851	0.04 Å
0.7934	0.10 Å

Table 3.3: Calculated pseudorotational g-factor of the ν_{18} mode of benzene; the correct result for a small vibration is obtained by extrapolating A at zero.

the $n = 0$ vibrational state, the result is simply:

$$\left\langle x^2 \right\rangle = \frac{\hbar}{m\omega}, \tag{3.12}$$

where m is the "mass" of the harmonic oscillator ($V(x) = (1/2)m\omega^2 x^2$).

In the present case we considered a small vibration, and $A(\theta)$ was chosen constant. We did not tried to estimate the amplitude of the vibration, as this calculations served us to test the applicability of our method to pseudorotations. Notice that in practical calculations, if $A(\theta)$ is too small, very accurate calculations are needed. We will come back to this, later in this work, when we will illustrate pseudorotations in solids.

A pseudorotation in benzene is expected to trigger orbital currents encircling the large molecular radius, and that might lead to unusually large magnetic screenings. Our calculated g-factor of benzene of about 0.79 (table 3.3) indicates instead for this pseudorotational mode a surprisingly modest 20% magnetic screening by the orbital electron currents.

In contrast, the rotational g-factor of benzene is slightly negative (ref. [1] reports the rotational g-factor of several ring molecules, derived from benzene; in all cases the g-factor is slightly negative). This is in agreement with the unusual large paramagnetic susceptibilty found in ring aromatic molecules, due to to the ring current induced by the magnetic field.

To understand the poor screening of the pseudorotation, we display in fig. 3.6 frames showing the evolution with θ of the electron charge density difference relative to undistorted benzene. Atoms pseudorotate counterclockwise, their small orbit causing large orbital electron currents with a complex

pattern.

The electron imbalance forms a sort of dipole – from the C–H bonds to the carbon ring– that rotates clockwise, while shifting phase, until at $\theta = \pi$ its sign has reversed – from the carbon ring to the C-H bonds. Moreover from $\theta = \pi$ until $\theta = 2\pi$ the charge motion occurs in reverse. The nearly exact balance of positive and negative currents explains the globally small magnetic screening in benzene. According to our calculated g-factor, a magnetic field should theoretically lead to a splitting of this E_2 mode:

$$\delta\nu_{18} = g \times 7.622 \text{ MHz } \frac{B}{\text{Tesla}}. \tag{3.13}$$

For a field of 10 Tesla the calculated splitting is only a tiny 59.8 MHz, when compared with a reported line width of about 500 GHz even below 50 K[45].

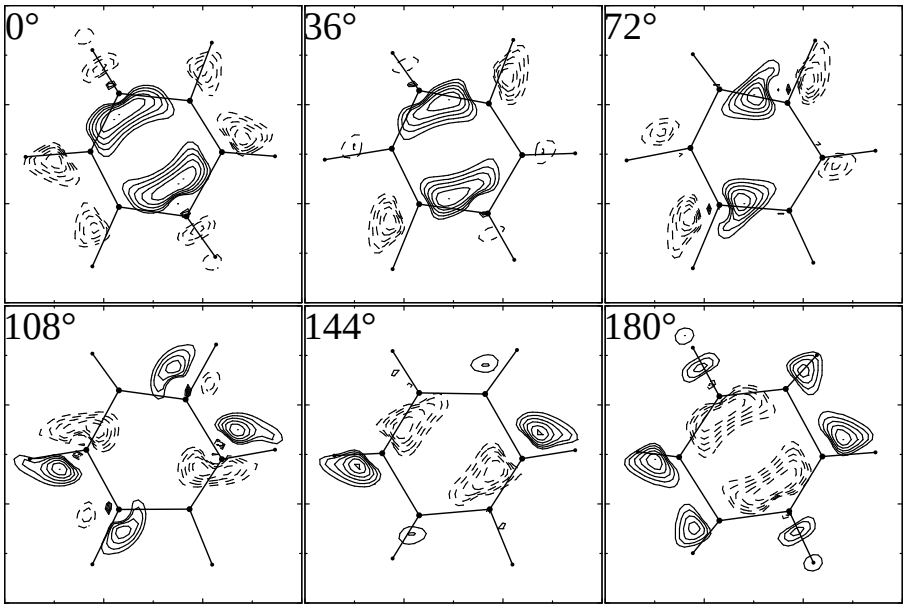

Figure 3.6: Illustration of orbital current caused by a pseudorotation in benzene. Plot shows the difference between distorted and undistorted electron density in the molecular plane at increasing values of the phase θ of the counterclockwise ion pseudorotation. Full lines: electron accumulation; dashed lines: electron depletion. Interval between isocharge lines: $4 \cdot 10^{-5}(au)^{-2}$. Carbon displacement amplitude 0.1 Å, here enhanced by a factor 5 for clarity. Note the clockwise motion of electron accumulation, and its phase shift into a depletion at $\theta = \pi$. The current is basically reversed from $\theta = \pi$ to $\theta = 2\pi$, explaining a relatively small magnetic screening (see text).

Chapter 4

Localized basis set calculations

The calculations in the previous chapter were carried out with a plane wave basis set. Even though plane waves are an excellent basis set for describing periodic systems, calculations done with this technique can be computationally intensive and may require massively parallel machines if the number of atoms is greater than 50-100. This is especially true when first row atoms or transition metal atoms are present, as they require a cutoff of ~ 80 Ry with standard norm-conserving pseudopotentials.

In the following we illustrate an alternative approach to DFT, based on a localized basis set, aimed at simpler and faster evaluation of the rotational and pseudorotational g-factors, still applicable to isolated molecules and to periodic systems.

4.1 The *SIESTA* approach to DFT

This section describes the self-consistent density-functional method implemented in the code *SIESTA* (Spanish Initiative for the Electronic Structure of Thousands of Atoms) [46, 47].

This method is based on the pseudopotential approximation, but unlike the plane-wave method, wavefunctions are expanded in a localized basis set, made up of atomic orbitals centered on each atom in the simulation cell. The

atomic orbitals are obtained by the solution of the radial Schrödinger equation of the pseudo-atom, with the additional constraint that these solution vanish beyond a certain cut-off radius r_c (confinement radius). The purpose of the confinement of the wavefunctions is to improve the convergence of the calculation going from the isolated atom to the solid. In fact, when two or more atoms become closer together, the exclusion principle dictates that the atomic wavefunctions get compressed and increase their kinetic energy [48].

Within the standard-pseudopotential approximation, the Kohn-Sham hamiltonian can be written as:

$$H = T + \sum_I \left[V_I^{loc}(\mathbf{r}) + V_I^{nl}\right] + V_H(\mathbf{r}) + V_{XC}(\mathbf{r}), \tag{4.1}$$

where I is an atom index, T is the kinetic energy operator, $V_H(\mathbf{r})$ and $V_{XC}(\mathbf{r})$ are respectively the Hartree and exchange-correlation potentials; V_I^{loc} and V_I^{nl} are the local and non-local (Kleinman-Bylander) parts of the atomic pseudopotentials of atom I.

In order to eliminate the long range part of $V_I^{loc}(\mathbf{r})$, which hamper unfeasible any calculation of periodic systems, the local potential is screened by an atomic electron density $\rho_I^{atom}(\mathbf{r})$ centered on the same site, constructed with appropriate valence atomic charges. The sum of the local potential $V_I^{loc}(\mathbf{r})$ and the Hartree and XC potentials arising from this atomic electron density, form the "neutral-atom" potential V_I^{na}. Notice that, since the atomic basis orbitals vanish beyond r_c, the screened neutral-atom potentials V_I^{na} are also zero beyond this radius.

Let now $\delta\rho(\mathbf{r})$ be the difference between the self-consistent electron density $\rho(\mathbf{r})$ and the sum of the atomic densities $\rho_I^{atom}(\mathbf{r})$. $\delta\rho(\mathbf{r})$ represents the change in electron density due to bonding and the charge transfer between the atoms. The Kohn-Sham hamiltonian can be rewritten as:

$$H = T + \sum_I V_I^{nl} + \sum_I V_I^{na} + \delta V_H(\mathbf{r}) + V_{XC}(\mathbf{r}). \tag{4.2}$$

The matrix elements of the first two terms involve only two-center integrals that can be precalculated at the beginning as a function of the nuclear separation between any two atoms.

The matrix elements of the three remaining terms are easily evaluated on a fine real space grid; this is the same grid needed for representing the charge density in the plane wave methods. Once the density is available at the grid points, V_{XC} is evaluated directly and δV_H is evaluated by fast Fourier transform. The hamiltonian (whose matrix size is the number of basis functions) is diagonalized by standard linear algebra methods or by sparse-matrix techniques and a new $\delta\rho(\mathbf{r})$ is obtained; the $\delta\rho(\mathbf{r})$ is then iterated to self-consistency.

4.2 Peierls' phase

Consider a wavefunction $\psi_{\mathbf{R}}(\mathbf{r})$ for a non-degenerate level of an atom located at position $\mathbf{R}$. Translation in a field is accompanied by a phase factor [49]:

$$\psi_{\mathbf{R}}(\mathbf{r}) = \psi_0(\mathbf{r}-\mathbf{R}) \exp\left[\frac{ie}{c}\Phi(\mathbf{R}\to\mathbf{r})\right], \tag{4.3}$$

where $\psi_0(\mathbf{r}-\mathbf{R})$ is the atomic wavefunction centered in $\mathbf{R}$; and $\Phi(\mathbf{R}\to\mathbf{r})$ is the integral of the vector potential along the straight line connecting $\mathbf{R}$ to $\mathbf{r}$. This expression is valid in the Landau or symmetric gauge, in which $\mathbf{A}$ is a linear function of $\mathbf{r}$.

For a very localized state the magnetic phase factor can be included in a tight-binding or LCAO form:

$$\Psi(\mathbf{r}) = \sum_k c_k \exp\left[\frac{ie}{c}\Phi(\mathbf{R}_k\to\mathbf{r})\right]\phi_k(\mathbf{r}-\mathbf{R}_k), \tag{4.4}$$

where k is the orbital index, $\mathbf{R}_k$ is the center of the k-th orbital, and $\Phi(\mathbf{R}_k\to\mathbf{r})$ is the phase associated with the center R_k.

The phase factor is constructed in such a way to cancel the vector potential term in the hamiltonian; in fact, the action of the hamiltonian on a basis function is:

$$\begin{aligned}\langle\mathbf{r}|\,H\,|k\rangle &= \left[\frac{1}{2m}\left(\mathbf{p}-\frac{e}{c}\mathbf{A}(\mathbf{r})\right)^2+V\right]\exp\left[\frac{ie}{c}\Phi(\mathbf{R}_k\to\mathbf{r})\right]\phi_k(\mathbf{r}-\mathbf{R}_k) = \\ &= \exp\left[\frac{ie}{c}\Phi(\mathbf{R}_k\to\mathbf{r})\right]\end{aligned}$$

$$\left\{\frac{1}{2m}\left[\mathbf{p}-\frac{e}{c}\left(\mathbf{A}(\mathbf{r})-\nabla\Phi(\mathbf{R}_k\to\mathbf{r})\right)\right]^2+V\right\}\phi_k(\mathbf{r}-\mathbf{R}_k)=$$
$$=\quad \exp\left[\frac{ie}{c}\Phi(\mathbf{R}_k\to\mathbf{r})\right]\left[\frac{\mathbf{p}^2}{2m}+V\right]\phi_k(\mathbf{r}-\mathbf{R}_k), \tag{4.5}$$

and then, under the assumption that the magnetic field is slowly varying respect to atomic distances, the matrix element of the hamiltonian, is obtained with the following Peierls' approximation:

$$\Phi(\mathbf{R}_k\to\mathbf{r})-\Phi(\mathbf{R}_{k'}\to\mathbf{r})\simeq\Phi(\mathbf{R}_k\to\mathbf{R}_{k'}), \tag{4.6}$$

where the integral of the vector potential is on the straight line from $\mathbf{R}_k$ to $\mathbf{R}'_k$. Thus the hopping matrix elements are renormalized by the so-called Peierls' factor:

$$H_{kk'}\to H_{kk'}\exp\left[\frac{ie}{c}\Phi(\mathbf{R}_k\to\mathbf{R}_{k'})\right], \tag{4.7}$$

$$S_{kk'}\to S_{kk'}\exp\left[\frac{ie}{c}\Phi(\mathbf{R}_k\to\mathbf{R}_{k'})\right]. \tag{4.8}$$

This Peierls phase approximation is valid for slowly varying magnetic field relative to atomic distances. It should only become equivalent to the exact London shifted basis [13] in the limit of infinitely localized basis functions, and is thus affected by an error proportional to the amount of delocalization.

Notice that the Peierls approximation, when used with only nearest neighbours interactions, yields always vanishing magnetic susceptibility except when there are closed loops, like in benzene or nanotubes; next-nearest neighbours interactions are equivalent to closed loops. The reason for vanishing magnetic susceptibility is that all the phase factors compensate and the spectrum of the hamiltonian is left unchanged by the magnetic field and:

$$\chi_{ij}=\frac{\partial^2 H}{\partial\mathbf{B}_i\partial\mathbf{B}_j}=0. \tag{4.9}$$

The Berry phase instead does not vanish, as the Peierls phase factors are still present in the wavefunction 4.4.

4.3 Technical details of the calculations

The Periels phase formalism is a non perturbative technique and there is no need to perform a linear response calculation, but only standard matrix diagonalizations. From the coefficients of the expansion of the wavefunctions on the localized basis set, the perturbation dependent wavefunction 4.4 is set up. We used the symmetric gauge ($\mathbf{A} = (1/2)\mathbf{B} \times \mathbf{r}$) with origin in the center of mass of the molecule.

In order to calculate the Berry phase, we followed a procedure similar to that for plane waves: the practical computation of the Berry phase consists in a sequence of calculations for many rotated configuration of the molecule. The angle increment was 6° ($\pi/30$). In calculating the discrete Berry phase (eq. 2.35) and the overlap matrix $\mathcal{S}_{ij}$ between occupied states (see eq. 2.36, not to be confused with the overlap matrix $S_{kk'}$ between basis functions), we applied again the Peierls approximation 4.6 to all the matrix elements between basis functions centered on different atoms.

Even if molecules are isolated systems, they were placed in the same periodically repeated cubic cell as for the plane wave case. We used the same norm-conserving pseudo-potentials and the same LDA functional as in the previous calculations based on plane waves; as before, the charge density was expanded up to a kinetic energy of 320 Ry.
We used three sets of basis functions:

- single-ξ (SZ): it is the minimal basis, containing one function for each occupied angular momentum channel (i.e. 1s for H, 2s 2p for C, ...);
- double-ξ (DZ): it contains two functions for angular momentum channel (i.e. 1s 2s for H, 2s 2p 3s 3p for C, ...);
- double-ξ plus polarization (DZP): in addition to the DZ basis set, it contains an extra basis function for each angular momentum up to $l = 2$ (i.e. 1s 2s + 3s 2p 3d for H, 2s 2p 3s 3p + 4s 4p 3d for C, ...).

The confinement radius is chosen automatically by the program in order to have a kinetic energy shift of 15 mRy on each orbital.

4.4 Results for rotational g-factor of molecules

We repeated calculations for all molecules considered earlier, and obtained the rotational g-factors summarized in table 4.1. Though clearly less accurate, the agreement with experiment and with the plane wave calculations is still quite good. Interestingly, the simplest minimal basis set SZ calculations, including just one function per angular momentum channel, gives the best results.

In particular, in CF_4 where the g-factor is marginally negative, the bigger DZP calculation fails to reproduce the overscreening but the SZ gets it. When using larger basis sets, the excited states are more diffuse and the Peierls approximation is evidently worse.

Altogether the localized basis calculations require much less computational effort than the plane wave ones. In our case, the CPU time required was 4 to 5 times smaller; and for bigger molecules the ratio is expected to increase. Moreover the memory requirements are far smaller, since only the charge density need to be stored in full detail in a real space mesh (in a plane wave code, instead, also the wavefunctions have to be stored in a reciprocal space mesh, dual to the real space mesh). This advantage should make that method preferable for larger size problems where the plane wave approach becomes impractical.

screening	**g-factor**	**basis set**
H_2^+ rotation:		
−5.43%	0.9457	PW
−5.89%	0.9411	SZ
−8.85%	0.9115	DZ
−6.41%	0.9359	DZP
H_2 rotation:		
−12.13%	0.8787	Expt. [2]
−12.45%	0.8755	PW
−12.35%	0.8765	SZ
−17.42%	0.8258	DZ
−13.06%	0.8694	DZP
C_2H_2 rotation:		
−92.9%	0.0490	Expt. [3]
−94.2%	0.0405	PW
−88.8%	0.0782	SZ
−98.0%	0.0139	DZP
CF_4 rotation:		
−106.6%	−0.0312	Expt. [3]
−109.4%	−0.0445	PW
−103.2%	−0.0151	SZ
−98.3%	+0.0080	DZP
CH_4 rotation:		
−68.7%	0.3133	Expt. [1]
−79.6%	0.2047	PW
−78.1%	0.2192	SZ
C_6H_6 pseudorotation:		
	0.7596	SZ, ampl. 0.02 Å
	0.7593	SZ, ampl. 0.04 Å
	0.7595	SZ, ampl. 0.10 Å
	0.7934	PW, ampl. 0.10 Å

Table 4.1: Localized basis set g-factors for various molecules: SZ, DZ and DZP denote the basis set used for the LCAO expansion of the wavefunctions.

Chapter 5

Quantum paraelectrics and ferroelectrics

In the second part of this thesis we wish to apply our new method for calculating the g-factor of pseudorotations in solids. Our chosen examples will be ferroelectric perovskites, where the soft phonon mode is degenerate and has the character of a pseudorotation, and must therefore give rise to a small magnetic moment. As a consequence of that, it will be split by an external magnetic field, and that can lead among other things to field-induced change of dielectric constant. Evaluation of the magnitude of this change requires precisely a calculation of the pseudorotational g-factor caused by magnetic screening of the electrons, which is unknown. Because the splittings are expected to be small, the phenomenon could be detectable in systems where the dielectric constant is very high, namely incipient ferroelectrics or quantum paraelectrics.

In this chapter we shall give first of all a brief description of the phenomenology of quantum paraelectrics and ferroelectrics, and we will focus our attention on two perovskites: potassium tantalate ($KTaO_3$) and strontium titanate ($SrTiO_3$). These crystal have very high static dielectric constants ($> 10^3$) and are incipient ferroelectrics, or "quantum paraelectrics" [8, 50].

We recall that the transition of a classical ferroelectric to a quantum to

paraelectric can be seen as a case of "rotational quantum melting" [51]. In the ferroelectric, the pseudorotation consists of the crystal cell polarization jumping between one preferred direction, or "valley", to another, then to yet another, and so on, until returning to the origin. In the paraelectric, the pseudorotation is the soft ferroelectric T_{1u} phonon mode. We will then need to discuss the crystal dynamical matrix in a magnetic field.

5.1 The perovskite structure

The general chemical formula for a perovskite is ABO_3. The ideal structure is cubic perovskite, where the A and B cations are arranged on a simple cubic lattice (as in the CsCl structure), and the O ions lie on the face centers nearest the (typically transition metal) B cations. Thus the B cations are at the center of BO_6 octahedra, while the A cations lie in a larger 12-coordinated site (fig. 5.1).

At high temperature, the ABO_3 perovskites retain full cubic symmetry. However, various structural phase transitions take place as the temperature is reduced. These may involve rotations and distortions of the BO_6 octahedra, as well as displacements of the cations from their ideal sites. The interplay of these instabilities accounts for the rich variety of ferroelectric and antiferroelectric behaviors. For examples, $BaTiO_3$ and $KNbO_3$ undergo phase transitions from the cubic paraelectric phase, to a succession of tetragonal, orthorhombic, and finally rhombohedral ferroelectric phases. In contrast, $PbTiO_3$ displays only a single transition from the cubic paraelectric phase to a tetragonal ferroelectric phase. In $NaNbO_3$ and $PbZrO_3$, nonpolar antiferrodistortive (AFD) or antiferroelectric (AFE) transitions take place, associated with different types of tilts of the oxygen octahedra.

The qualitative reason for ferroelectricity in these perovskites arises generally from B–O bonds that, due to the large size of cation A, are slightly too long in the undistorted phase. Upon distorting, one B–O bond becomes more covalent, shorter, and stronger, and this overcompensates for the loss of

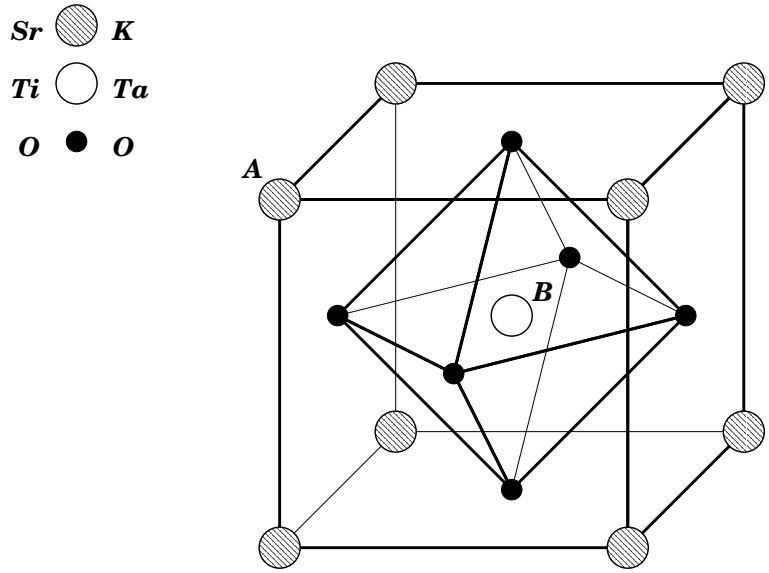

Figure 5.1: The cubic perovskite structure. The BO_6 octahedra are shown. The A cations lie in a 12-coordinated site

strength of all the others. Electronically, the high-symmetry valence bands are linearly split with a quadratic energy gain that could upper be viewed as a pseudo Jahn-Teller effect [5]. When the size of the cation A is reduced, ferroelectricity is instead gradually suppressed.

Incipient ferroelectrics (also called quantum paraelectrics [8, 50] because of the crucial role of quantum fluctuations in that case), are systems poised on the brink of ferroelectricity at zero temperature.

Ferroelectricity in perovskites is displacive, and generally associated with a "soft-phonon" mode, whose frequency drops to zero upon cooling, vanishes nominally at the ferroelectric transition, and hardens back again upon further cooling [52]. In incipient ferroelectrics the soft mode is exceedingly low in the range of 10–20 cm^{-1}, and ferroelectricity can be easily induced by driving it to zero with externals agents such as uniaxial expansion or doping.

The two perovskites under consideration in this work are strontium titanate ($SrTiO_3$) and potassium tantalate ($KTaO_3$). Both behave as incipient ferroelectrics [8], in the sense that they have a large static dielectric response

and as temperature is reduced, the static dielectric response closely obeys a Curie-Weiss law of the form:

$$\epsilon \sim (T - T_c)^{-1}, \tag{5.1}$$

but the divergence at the critical temperature T_c that would be expected from this formula is not observed. Instead, the static, lattice-induced dielectric susceptibility saturates at an enormous value ($\sim 2 \cdot 10^4$ for $SrTiO_3$) as T approaches to zero (fig. 5.4).

Regarding structure, $KTaO_3$ retain its cubic structure down to very low temperature, while $SrTiO_3$ undergoes a non-ferroelectric phase transition from the cubic to a tetragonal antiferrodistorted (AFD) phase when temperature drops below 105 K. This is due to a softening of the lowest frequency triply degenerate zone-corner R-point vibrational mode. In this mode, the Sr and Ti atoms remain fixed, while the oxygen octahedra rotate about one of the cubic axes passing through the Ti atom, in opposite senses in all adjacent cells, as shown in fig. 5.2. This rotation of the oxygen octahedra is coupled to lattice strain and the crystal structure passes from cubic to tetragonal, slightly compressing in the direction parallel to the rotation axis, and slightly expanding in the plane perpendicular to that axis. The new crystal cell thus contains two formula unit and it is shown in fig. 5.3; the new lattice vectors are chosen along the [110], [$\bar{1}$00] and [001] directions of the original cubic structure.

5.2 Quantum paraelectrics

In this section, we will give a phenomenological review of the physics of quantum paraelectrics [8, 50, 53, 54, 55].

At high enough temperature, the perovskites $SrTiO_3$ and $KTaO_3$ behave just like ordinary classical paraelectrics, well described by the displacive limit, with very well defined optically active TO modes, hard and narrow. These modes soften down upon cooling, as expected in analogy with ordinary ferroelectrics like $BaTiO_3$.

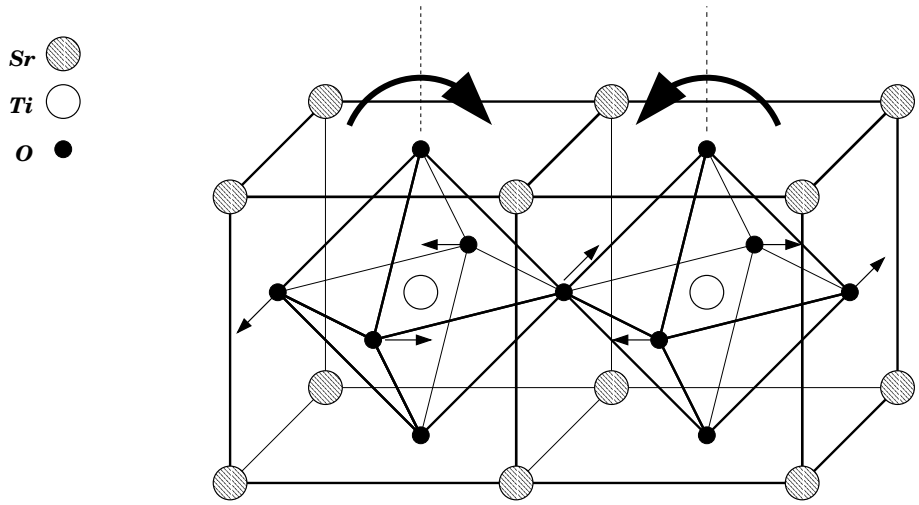

Figure 5.2: Displacement pattern generating the AFD instability in the cubic structure on $SrTiO_3$. The oxygen octahedra rotate about one cubic axis in opposite sense in all adjacent cells.

However, just above the extrapolated classical Curie temperature (37 K for $SrTiO_3$, and 40 K for $KTaO_3$), the picture changes. In $SrTiO_3$ the soft mode levels off and broadens. Müller and coworkers [50] observed a dip at 37 K of the EPR spin hamiltonian of a Fe^{3+} impurity, indicating a weak phase transition. Also experimental observations of hyper-Rayleigh scattering indicates the presence of local disorder, or off-center displacement of the ions, which locally breaks the inversion symmetry. Various anomalies observed in the spectroscopy of soft and acoustic modes in $SrTiO_3$ point to the existence of large clusters, whose typical size equals the wavelength of the reduced wavevector for which the anomalies are most pronounced ($\lambda \sim 20$ lattice constants at very low T) [1]).

In $KTaO_3$, the NMR experiments clearly indicate a dynamical off-center displacement of the Ta ions which sets up rather abruptly below 40 K [57]. In the microwave region, the slow Debye relaxations typical of the order-disorder regime appear in $KTaO_3$, their typical frequency τ^{-1} decreasing with

[1] for a review, see [56]

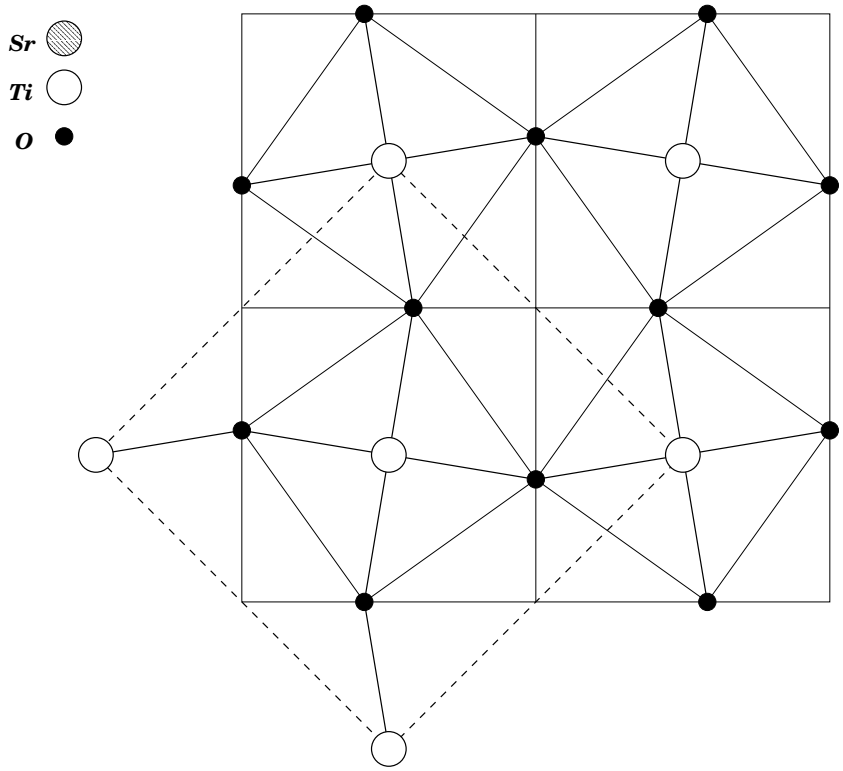

Figure 5.3: Sketch of the structure of tetragonal AFD phase of $SrTiO_3$. View is along the tetragonal axis. Only the Ti–O_2 plane is shown. The rotation of the oxygen octahedra has been enhanced for sake of clarity. The dashed lines indicate the new tetragonal cell.

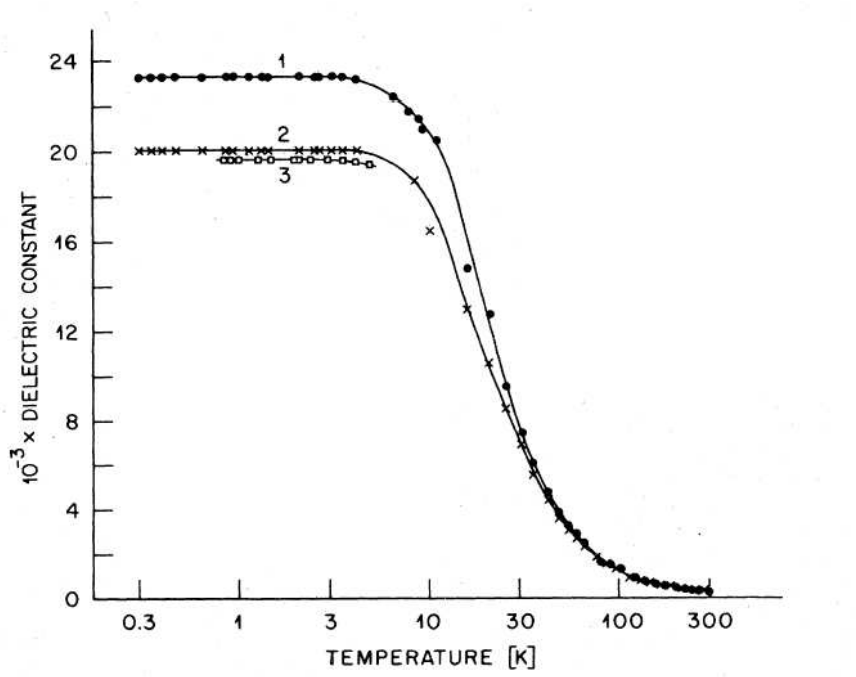

Figure 5.4: Dielectric constant as a function of temperature for three samples of $SrTiO_3$ [8].

temperature. Unlike the classical systems, however, τ doesn't diverge with decreasing temperature, but saturates to a very long relaxation time ($\tau^{-1} \sim$ 500 MHz). Because of this lack of divergence of τ, long-range ferroelectric order is never reached, and the system remains paraelectric even at the lowest temperatures. The failure to order ferro electrically accompanied by these slow dielectric fluctuations has been attributed to quantum zero-point motion of the ions [8].

The reason why zero point motion and quantum fluctuations are so important in $SrTiO_3$ and $KTaO_3$ is not because the ions are particularly light. Rather, the lattice spacing is so tight, as compared e.g. to $BaTiO_3$, to leave very little room for the Ti or Ta ions to move off-center and form a preferential strong covalent bond with one of the surrounding oxygen atoms. As the lattice is compressed, the classical ferroelectric off-center equilibrium

displacement gets smaller and smaller and the system approaches the classical displacive limit, characterized by a vanishing Curie temperature and a vanishing zero temperature distortion magnitude. The extrapolated classical off-center Ti displacement is only ~ 0.03 Å at low temperature in $SrTiO_3$, against ~ 0.1 Å in $BaTiO_3$. As the equilibrium classical displacements gets smaller and smaller, the influence of zero-point quantum mechanical motion increases, because the off-center valleys get shallower, and the barrier separating the different valleys decreases. The limit where this barrier drops to zero is entirely dominated by quantum effects, with quantum fluctuations acting to suppress ferroelectricity well before its classical disappearance [53, 54, 51].

The quantum fluctuations can be easily removed, the system reverting into a regular ordered ferroelectric, by applying either pressure or impurity doping, as in the case of $KNb_xTa_{1-x}O_3$ [58].

Other remarkable systems where the suppression of ferroelectricity is caused by quantum fluctuations do exist: one of them is potassium dihydrogen phosphate (KDP), whose chemical formula is KH_2PO_4 [59, 55], under pressure.. The paraelectric structure of KDP is a body-centered tetragonal arrangement of $K_2P(OH)_4$ distorted octahedral units. The $-OH$ groups of neighboring units are linked together by hydrogen bonds. In the high temperature paraelectric phase the hydrogens form a covalent bond plus an hydrogen bonds between two oxygen atoms. Under pressure, the hydrogens move to a bond-center position, pulling the two bridge oxygens together, the whole lattice volume shrinking by a few percent, suppressing ferroelectricity.

5.3 Rotational quantum melting in $KTaO_3$ and $SrTiO_3$

In the displacive model of classical ferroelectrics, the B atom goes off-center driven by the formation of a strong covalent bond with one of the equivalent surrounding oxygens, and an electric dipole appears in the B–O direction. When the off-center displacement becomes small, the central atom can tun-

nel between the six (or four, depending on the lattice symmetry) equivalent potential energy valleys. As these quantum fluctuations, which are proportional to the intra-cell inter-valley tunnel splitting, become stronger than the ferroelectric inter-cell interaction, then a quantum paraelectric state can be stabilized even at zero temperature: quantum mechanical rotation of the B ion around the center being the driving force.

Perovskite quantum paraelectrics are in this sense a case of "rotational quantum melting"; unlike classical melting, there is deep order in the quantum melted ground state. Here we will review some concepts out forward by Tosatti and Martonák [51].

Each B–O dipole bond, once formed by lowering temperature, can take a multiplicity of orientations inside the oxygen cage, and therefore may be seen as a discrete rotor. The cubic field of the crystalline cage leaves angular momentum of the lowest lying states, $L = 0$ for the ground state, and $L = 1$ for the first excited state (call their energy separation Δ) unquenched. If a large ferroelectric coupling J between different cells is present, hybridization between different L states of neighboring cells becomes dominant. In the ensuing ferroelectric ordered state, rotational symmetry is broken and individual angular momentums are quenched.

For sufficiently small $J \ll \Delta$, however, it becomes more convenient to disrupt ferroelectric order, and to recover rotational invariance as in the $J \to 0$ limit. In this limit the ground state is just a product of $L = 0$ states in each cell, it is non degenerate, and has a finite excitation gap Δ. For finite but small J, the gap will decrease, but symmetry will not change, at zero temperature, until a critical value $(J/\Delta)_c$, where the gap closes, and ferroelectricity sets in. Conversely, starting from the ferroelectric regime and decreasing J, there is rotational quantum melting at $T = 0$ to a quantum paraelectric when $(J/\Delta)_c$ is reached.

5.4 Soft modes as quantum rotors

Within the soft mode theory of phase transitions, the structural phase transition takes place when the lowest frequency vibrational mode goes unstable, and thus the system breaks its symmetry and distorts along the direction of the soft mode. The undistorted configuration is no more a minimum in the potential energy surface, and due to the cubic crystal field generated by the neighboring oxygens, the actual potential energy surface shows that there are potential energy valleys and mountains, the former situated off-center, in the direction of the six B–O bonds. When the central atom sits off-center, an electric dipole arises, in the direction of the six B–O bonds [52].

The 3-fold degenerate soft mode in cubic perovskites, correspond to the three orthogonal directions along which the metal atom goes off-center; moreover, the 3-fold T_{1u} mode has the same group symmetry properties of a $L = 1$ three-dimensional rigid rotator. This analogy between soft-modes and quantum rotors, will be emphasized when evaluating the effect of an external magnetic field on the T_{1u} soft-mode in perovskites, and the dependence of the static dielectric constant upon the applied magnetic field.

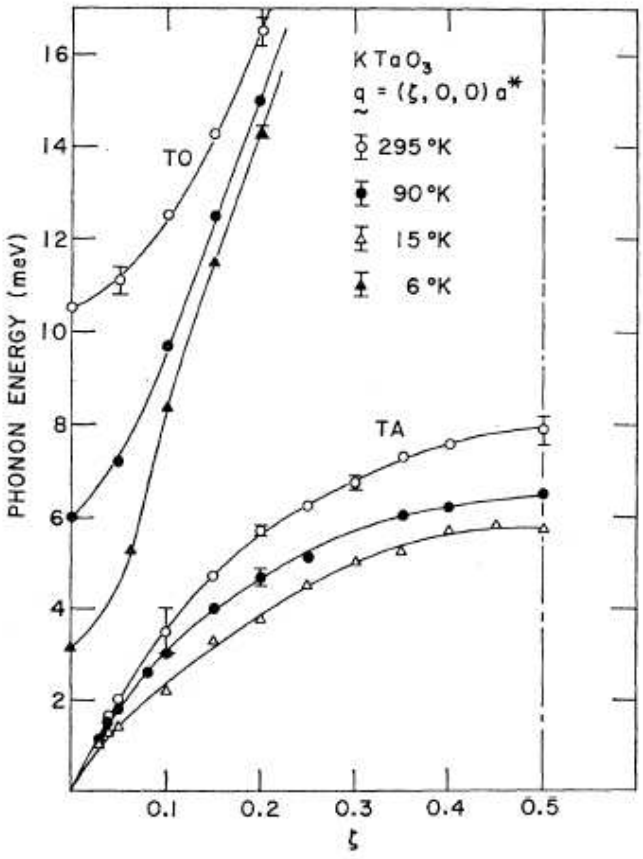

Figure 5.5: Temperature dependent phonon spectrum of $KTaO_3$, measured by neutron diffraction. TO = transverse optic phonon (soft mode); TA = transverse acoustic phonon.

Chapter 6

Pseudorotations in solids: ferroelectric perovskites

In this chapter we will show the results of Berry phase calculations of the pseudorotational magnetic g-factor for the soft mode of $KTaO_3$ and $SrTiO_3$ in their paraelectric or incipient ferroelectrics state. In order to apply the integral formulation of magnetic screening, it is necessary to determine the trajectory followed by the pseudorotating nuclei. The actual trajectory is well approximated by the soft phonon eigenvectors on the paraelectric side, and by adiabatic potential energy "valley" on the ferroelectric side of the phase diagram. These two trajectories are in any case very similar in shape; the size is however microscopic in the paraelectric state, but macroscopic in the ferroelectric state.

Experimentally, $KTaO_3$ can be made ferroelectric by applying a uniaxial stress; the lattice shrinking in one direction is accompanied by the lattice expansion in the two orthogonal direction, and ferroelectricity develops on the plane perpendicular to the applied stress [60]. On the contrary, $SrTiO_3$ at low temperature undergoes a phase transition from cubic to a tetragonal antiferrodistortive (AFD); theoretically, the low temperature tetragonal phase is classically unstable [61] to two orthogonal ferroelectric modes ($A + 2E$). In both cases, ferroelectric $KTaO_3$ under uniaxial stress [001] and tetragonal

AFD $SrTiO_3$, the threefold degenerate soft mode splits into a twofold degenerate E mode and a nondegenerate A mode. The pseudorotation generated by the E mode lies on the (001) plane. We used this twofold degenerate E mode in our calculation of the adiabatic potential energy surface.

6.1 Dynamical matrix in a magnetic field

In order to evaluate the effect of an applied magnetic field on the soft mode frequency and eigenvectors, the equations of motion for the bare ions must take into account the Lorentz force term coming from the magnetic field. Let the magnetic field be oriented in the z direction, and let $u_\alpha(l)$ the displacement of the atom l in direction $\alpha = x, y, z$, with respect to the equilibrium positions. In a simple two-body force approximation and disregarding out first electrons, the equations of motion are:

$$\begin{cases} M_l \ddot{u}_1(l) = -\sum_{l'\alpha'} \Phi_{1\alpha'}(ll') u_{\alpha'}(l') + (Z_l B/c)\dot{u}_2(l) \\ M_l \ddot{u}_2(l) = -\sum_{l'\alpha'} \Phi_{2\alpha'}(ll') u_{\alpha'}(l') - (Z_l B/c)\dot{u}_1(l) \\ M_l \ddot{u}_3(l) = -\sum_{l'\alpha'} \Phi_{3\alpha'}(ll') u_{\alpha'}(l'), \end{cases} \tag{6.1}$$

where:

$$\Phi_{\alpha\alpha'}(ll') = \frac{\partial^2 E}{\partial u_\alpha(l) \partial u'_\alpha(l')} \tag{6.2}$$

is the force constants matrix. In principle, the external magnetic field affects also the electronic structure of the system and the force constants will depend themselves from the magnetic field. But for small magnetic fields (< 30 Tesla), that can be reached in laboratory, the magnetic field can be treated as a small perturbation to the crystal potential, and the charge density remains unchanged, to first order in the field. As a consequence of this, the Hellman-Feynman forces do not depend from the magnetic field, at least to first order.

After making the substitution $u \to u \exp[i(\omega t + k \cdot x)]$, and setting $k = 0$ as we are interested in the zone center phonons, we get:

$$\begin{cases} \omega^2 e_1(l) = \sum_{l'\alpha'} D_{1\alpha'}(ll') e_{\alpha'}(l') - i\omega \frac{Z_l B}{M_l c} e_2(l) \\ \omega^2 e_2(l) = \sum_{l'\alpha'} D_{2\alpha'}(ll') e_{\alpha'}(l') + i\omega \frac{Z_l B}{M_l c} e_1(l) \\ \omega^2 e_3(l) = \sum_{l'\alpha'} D_{3\alpha'}(ll') e_{\alpha'}(l'), \end{cases} \tag{6.3}$$

where:

$$D_{\alpha\alpha'}(ll') = \frac{\Phi_{\alpha\alpha'}(ll')}{\sqrt{M_l M_{l'}}}, \tag{6.4}$$

is the unperturbed dynamical matrix and

$$e_\alpha(l) = \sqrt{M_l}\, u_\alpha(l). \tag{6.5}$$

In matrix form, the previous system of equations becomes:

$$\omega^2 \underline{\underline{I}}\, \underline{e} = \underline{\underline{D}}\, \underline{e} + i\omega(B/c)\underline{\underline{E}}\, \underline{e}, \tag{6.6}$$

where the matrix $\underline{\underline{E}}$ has this simple form:

$$\underline{\underline{E}} = \begin{pmatrix} 0 & -Z_1/M_1 & 0 & & & & \\ Z_1/M_1 & 0 & 0 & & & & \\ 0 & 0 & 0 & & & & \\ & & & 0 & -Z_2/M_2 & 0 & \\ & & & Z_2/M_2 & 0 & 0 & \\ & & & 0 & 0 & 0 & \\ & & & & & & \ddots \end{pmatrix}. \tag{6.7}$$

In order to obtain perturbatively the frequency change of the soft mode, we take a linear combination of the threefold degenerate soft mode eigenvectors (call them $\underline{e}^{(i)}$, with $i = 1, 2, 3$, $e^{(i)}_\alpha(l) \neq 0$ only if $\alpha = i$):

$$q_n(l, \alpha) = \sum_{i=1}^{3} A_{n,i} e^{(i)}_\alpha(l). \tag{6.8}$$

In this new basis, the two matrices $\underline{\underline{D}}$ and $\underline{\underline{E}}$ become 3×3 matrices, given by:

$$\mathcal{D}_{m,n} = \sum_{i,j} A^\star_{n,i} A_{m,j} \sum_{l\alpha\, l'\alpha'} e^{(n)}_\alpha(l) D_{\alpha\alpha'}(ll') e^{(m)}_{\alpha'}(l') \tag{6.9}$$

$$= \omega_0^2 \sum_i A^\star_{n,i} A_{m,i}, \tag{6.10}$$

where ω_0 is the frequency of the soft mode in zero magnetic. The matrix $\underline{\underline{\mathcal{E}}}$ is real antisymmetric and in our geometry only $\mathcal{E}_{1,2}$ and $\mathcal{E}_{2,1}$ are different from zero:

$$\mathcal{E}_{1,2} = -\mathcal{E}_{2,1} = \tag{6.11}$$

$$= \sum_{i,j} A^\star_{n,i} A_{m,j} \sum_l \frac{Z_l}{M_l} e^{(1)}_1(l) e^{(2)}_2(l). \tag{6.12}$$

Eq. 6.6 can be rewritten as:

$$\frac{\omega^2 - \omega_0^2}{\omega} \underline{\underline{\mathcal{I}}}\, \underline{q} = i\, \frac{B}{c}\, \underline{\underline{\mathcal{E}}}\, \underline{q}, \tag{6.13}$$

which is a matrix eigenvalue equation; the eigenvectors give the rows of the $A_{i,j}$ matrix. The result is simply ($\Delta\omega \ll \omega_0$):

$$\Delta\omega = 0,\ \pm\frac{B}{2c} \sum_l \frac{Z_l}{M_l} e_1^{(1)}(l) e_2^{(2)}(l), \tag{6.14}$$

to linear order in B. Notice that in this equation, the eigenvectors $\underline{e}$ are normalized to one. The result is in fact independent from the area of the orbit, which is proportional to $1/\omega$, because the current generated by the orbital motion is proportional to ω. Of the three original modes, the one polarized parallel to the magnetic field is unaffected ($\underline{q}_3 = \underline{e}_3$). The other two modes ($\underline{q}_1 = \sqrt{2}/2(\underline{e}_1 - i\underline{e}_2)$, $\underline{q}_2 = \sqrt{2}/2(\underline{e}_1 + i\underline{e}_2)$), transverse to the field, are split by an amount proportional to the magnetic field. The splitting is:

$$\Delta\omega = \pm\mu_N B \sum_l \frac{Z_l}{m_l} e^{(1)}(l) e^{(2)}(l) \tag{6.15}$$

$$= 2.54 \cdot 10^{-4} \mathrm{cm}^{-1} g_{\mathrm{bare}} \frac{B}{\mathrm{Tesla}}, \tag{6.16}$$

where:

$$g_{\mathrm{bare}} = \sum_l \frac{Z_l}{m_l} e^{(1)}(l) e^{(2)}(l). \tag{6.17}$$

The last equation allows to calculate the splitting of the soft-mode due to the orbital motion of the bare nuclei; μ_N is again the nuclear magneton; m_l is the mass of the ion l in units of the proton mass and Z_l is the valence charge in units of the electron charge; g_{bare} is a pure number. The quantity $\mu_N g_{\mathrm{bare}}$ is then the bare nuclear orbital magnetic moment of the mode.

To first order in the magnetic field, the 3-fold degeneracy of the T_{1u} mode is removed in the same way the Zeeman term removes the degeneracy of the $L = 1$ state of the quantum 3D rigid rotator, or of a p state of the hydrogen atom (fig. 6.1). Notice that the linear splitting is valid only when the $\Delta\omega$ is much smaller than the soft mode frequency; when the soft mode frequency goes to zero, the splitting is no more symmetric.

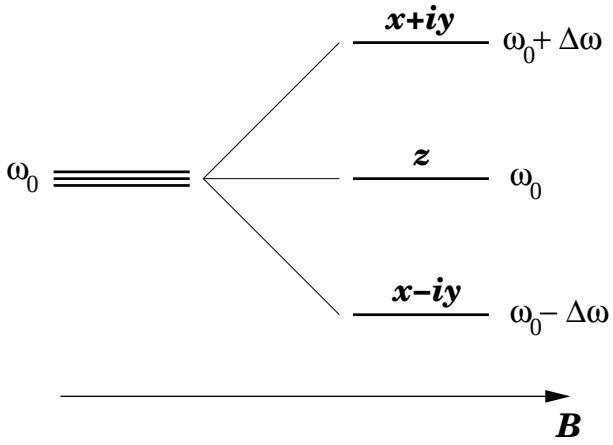

Figure 6.1: Magnetic field-induced splitting of the soft mode. $\Delta\omega$ is proportional to the magnetic moment. The pattern of splitting is the same of the Zeeman splitting on an $L = 1$ state.

Up to now we have considered the effect of the magnetic field on the bare nuclear charges, ignoring the electrons. As seen in earlier chapters, the effect of electrons within the Born-Oppenheimer approximation consist in adding a vector potential-like term to the canonical momentum of each ions (Berry connection). The Berry connection $\vec{\chi}$ enters the dynamical matrix as an additional Lorentz force-like term:

$$Z_l \dot{\mathbf{u}}(l) \times \frac{\mathbf{B}}{c} - \dot{\mathbf{u}}(l) \cdot \vec{\nabla}_l \vec{\chi}(l), \tag{6.18}$$

$$\vec{\chi}(l) = i \left\langle \psi \right| \vec{\nabla}_l \left| \psi \right\rangle . \tag{6.19}$$

Repeating the calculation taking into account this extra term, and equation 6.6 for the lattice dynamics becomes:

$$\omega^2 \underline{\underline{I}}\ \underline{e} = \underline{\underline{D}}\ \underline{e} + i\omega(B/c)\underline{\underline{E}}\ \underline{e} + i\omega \underline{\underline{F}}\ \underline{e}. \tag{6.20}$$

By specializing again to the threefold degenerate T_{1u} soft mode, the 3×3 matrix $\underline{\underline{\mathcal{F}}}$ is real antisymmetric:

$$\mathcal{F}_{nn} = 0, \quad \mathcal{F}_{nm} = -\mathcal{F}_{mn} \tag{6.21}$$

$$\mathcal{F}_{nm} = \sum_l \frac{1}{2M_l} e^{(1)}(l) e^{(2)}(l) \mathcal{Y}_{nm}(l), \tag{6.22}$$

where

$$\mathcal{Y}_{nm} = \frac{\partial \chi_n}{\partial u_m} - \frac{\partial \chi_m}{\partial u_n} = -2 \,\mathrm{Im} \left\langle \frac{\partial \psi}{\partial u_n} \middle| \frac{\partial \psi}{\partial u_m} \right\rangle \tag{6.23}$$

is the so-called Berry curvature, which is a gauge invariant and in principle physically observable [15]. The Berry curvature is the analog of the magnetic field; in fact, the $n = 1, m = 2$ component is equal to the component of $\nabla \times \chi$ parallel to the applied magnetic field. The main difference with respect to the physical magnetic field, is that the Berry connection is not uniform in space. The new splitting $\Delta\omega$ of "$L = \pm 1$" is given by:

$$\Delta\omega = \pm \frac{1}{2} \sum_l \left[\frac{B \; Z_l}{M_l c} + \frac{\mathcal{Y}_{12}(l)}{2M_l} \right] e^{(1)}(l) e^{(2)}(l), \tag{6.24}$$

and is still linear in the external field B, since $\mathcal{Y}_{mn}$ is proportional to A/c.

As pointed out by Resta [18], a computation of the Berry curvature could be actually implemented, but it would require the evaluation of all the excited states at any point in parameter space. Once again, it is wiser to resort to an integral formulation, by computing the Berry phase along a closed orbit, which equals the flux of the Berry curvature through the orbit. Then the pseudorotational g-factor is simply related to the bare one, by the usual relation:

$$g = (1 + \sigma) g_{\mathrm{bare}}, \tag{6.25}$$

where σ is the magnetic screening as defined in earlier chapters. The magnetic screening is evaluated by integrating the vector potential and the geometric vector potential terms around a closed loop in configuration space. The closed loop can be chosen as the classical trajectory of the nuclei on the potential energy surface. Later we will show that the combination of two of the degenerate T_{1u} eigenvectors with a simple phase factor generates a trajectory which is very close to the actual trajectory on the adiabatic potential energy surface.

6.2 $KTaO_3$ and $SrTiO_3$ cubic structure

Our task is now the calculation of g_{bare} and of the magnetic screening σ for incipient perovskite ferroelectrics, $KTaO_3$ and $SrTiO_3$. All the calculations on $KTaO_3$ and $SrTiO_3$ were performed with the plane wave pseudopotential method and in order to check the convergence needed for a correct representation of the wavefunctions, we performed a set of standard electronic structure calculations on the perfect cubic perovskite structure and compared to both experimental data and existing calculations in literature.

6.2.1 $KTaO_3$

We used standard norm-conserving Martins-Troullier [62] pseudopotentials for the three atomic species. They were generated in the same configuration and with the same cutoff radii as found in literature. The oxygen pseudopotential was generated according from Troullier and Martins [62], the p channel taken as local. The potassium pseudopotential was generated in the $4s^1 4p^0$ configuration with $r_s = 3.65a_0$, $r_p = 3.8a_0$. The s channel was taken local and the non-linear core correction was added to the potential [63]. The tantalum pseudopotential was generated in the $6s^2 6p^0 5d^3$ configuration with $r_s = 2.68a_0$, $r_p = 3.44a_0$ and $r_d = 1.51a_0$. As before, the s channel was taken as local [64].

We used a plane wave cutoff of 80 Ry, a Monkhorst-Pack (6,6,6) mesh [65] for sampling the Brillouin zone, and the Perdew and Zunger parametrization [23] of the LDA functional.

The LDA equilibrium lattice spacing was found to be 3.936 Å and the bulk modulus 192 GPa, to be compared to the experimental values of 3.983 Å and 218 GPa. The underestimation of the lattice spacing is well known for the LDA functional. We did not find in literature any other plane wave calculation of the same properties, but two full-potential (FP) studies of $KTaO_3$, one by Postnikov and coworkers [66, 67, 68] who used a FP-LMTO method and by D. J. Singh [69] who used a FP-LAPW method. These results

Lattice spacing (Å)	Bulk modulus (GPa)	Notes
3.983	218	Experiment
3.936	192	This work
3.928	225	FP-LMTO [67]
3.960	211	FP-LAPW [69]

Table 6.1: $KTaO_3$ lattice spacing and bulk modulus.

are summarized in table 6.1.

We also calculated the electronic band structure of cubic $KTaO_3$ (fig. 6.2). The nine valence bands are mainly derived from O $2p$ orbitals. These are separated by an indirect (R-Γ) gap from the transition metal d derived conduction bands. However, from the projected density of states [69], there is quite a large $p - d$ hybridization, reflecting the partial covalent of the Ta–O bond. As in typical LDA calculations for insulators, the bands gaps are underestimated. The calculated energy gap is 2.58 eV, to be compared with the experimental value of 3.8 eV.

As mentioned earlier, $KTaO_3$ does not undergo phase transitions and remains cubic down to low temperature. Experimentally, the zone center Γ_{15} softens by cooling, from 80 cm^{-1} at room temperature, to 24 cm^{-1} at 12 K [70] (see fig. 5.5).

Theoretically, the energetics of the ferroelectric instability is very sensitive to the Brillouin zone sampling, reflecting the importance of an accurate description of the metal-oxygen covalent bond, and particularly the sampling of the $\mathbf{k} \simeq 0$ region where the pseudo Jahn-Teller splitting occur. The ferroelectric instability is also very sensitive to volume; when a hydrostatic pressure is applied, the BO_6 cage get smaller and there is less room for the metal atom to move off-center thus destroying ferroelectricity. In fact, in ferroelectrics like $BaTiO_3$, the BaO_6 cage is somehow "expanded".

Not surprisingly therefore, the calculation of the frequency of the soft mode in perovskites is very sensitive to the volume of the cell. In general a

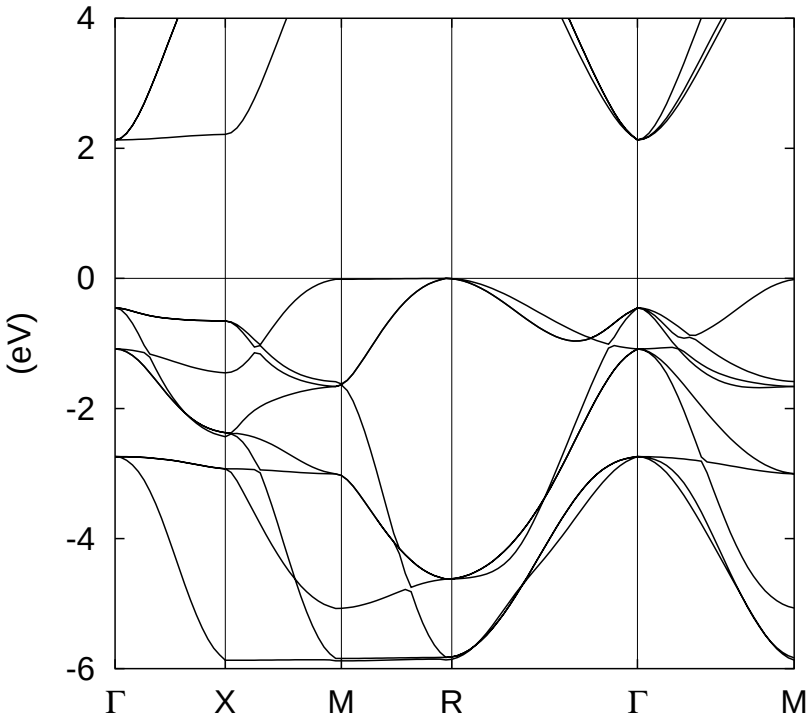

Figure 6.2: $KTaO_3$ band structure in the cubic perovskite structure.

Mode	**Exp. (12 K)** [70]	**This work**	**FP-LMTO** [68]	**FP-LAPW** [69]
T_{1u}	24	107	$61i$	80
T_{1u}	196	215	205	172
T_{1u}	546	602	504	528
T_{2u}	279	288	330	264

Table 6.2: Calculated and experimental phonon frequencies in cm^{-1} for $KTaO_3$ at the experimental lattice spacing.

calculation done at the theoretical equilibrium lattice spacing, which in LDA tends to be smaller than the experimental one, predicts the soft mode to be stable (i.e. positive ω^2). The same calculation done at the experimental lattice spacing, which is a bit larger, might instead predict a lattice instability (i.e. negative ω^2), and thus a ferroelectric state [71, 72, 61]. Our finding of the absence of the ferroelectricity in $KTaO_3$, in agreement with experiment, is gratifying and expected, since LDA calculations generally agree best with experiment when performed at the experimental lattice.

The calculated zero field, zero temperature T_{1u} and T_{2u} phonon frequencies at the experimental lattice spacing are shown in table 6.2. The frequency of the three T_{1u} modes are higher with respect to the experimental values and to FP calculations. But most important, the soft mode is predicted to be stable even at the experimental lattice spacing, like in the calculation by Singh and contrary to the findings of Postnikov and coworkers. These results underline the extreme sensitivity of the soft mode frequency not just to volume, but to all details and approximations. The eigenvectors however appear to be more stable: and the are what will give us a dependable g-factor.

6.2.2 $SrTiO_3$

Strontium titanate was studied theoretically in detail by Vanderbilt and coworkers [71, 61, 73]. In order to build on this well-documented case, we

decided to take as reference precisely the calculations of Sai and Vanderbilt [61], using the same technique and working in the same conditions. The ultrasoft [74] pseudopotentials for the three atoms, were kindly provided by Prof. Vanderbilt. Each pseudopotential contains two non-local projectors per angular momentum channel. The Sr pseudopotential was generated in the $4s^2 4p^6 5s^2$ configuration and includes the $4s, 4p$ semicore states; the Ti pseudopotential was generated in the $3s^2 3p^6 4s^2 3d^1$ configuration and includes the $3s, 3p$ semicore states.

We used the same plane wave cutoff of 30 Ry for the wavefunctions and 270 Ry for the charge density, as Vanderbilt. By using the same Brillouin zone sampling, the (6,6,6) Monkhorst-Pack mesh, we got of course identical results for the lattice spacing and bulk modulus. The structure is found to be stable at the LDA lattice spacing, while at the experimental lattice spacing it is unstable against both the zone center soft ferroelectric mode and zone border antiferrodistortive (AFD) mode.

Fig. 6.3 shows the band structure in the perfect cubic structure and in the ferroelectric distorted structure (but not the AFD distorted structure). The main difference between the two sets of bands are in the region around the Γ point and are shown in of fig. 6.4. The ferroelectric splitting is larger for the conduction band, and it extends along the $\Gamma - R$ direction up to zone border. The doubly degenerate valence band are split at Γ and, they cross along the $\Gamma - R$ at a wavevector $\delta k^{-1} \simeq 4$ lattice cells. This is a rough estimate of the correlation length of ferroelectricity for this distortion, which means, the typical size of clusters of rotors in $SrTiO_3$.

Furthermore, the energy gain caused by the distortion is proportional to the energy splitting times the volume in k-space where the pseudo Jahn-Teller splitting appears. From fig. 6.4, the splitting is anisotropic and affects mainly the $\Gamma - R$ line and the region of k-space interested by the pseudo Jahn-Teller is an ellipsoid elongated in the $\Gamma - R$ direction. The volume in the Brillouin zone could be taken roughly proportional to δk, which in turn

is itself proportional to ΔE, the pseudo-JT splitting[1].

[1]That would make the energy gain of order $(\Delta E)^2$, which is the same power but the opposite sign of the elastic cost of the distortion. An accurate calculation will require very fine BZ sampling and the calculation of energy gain as a function of the distortion

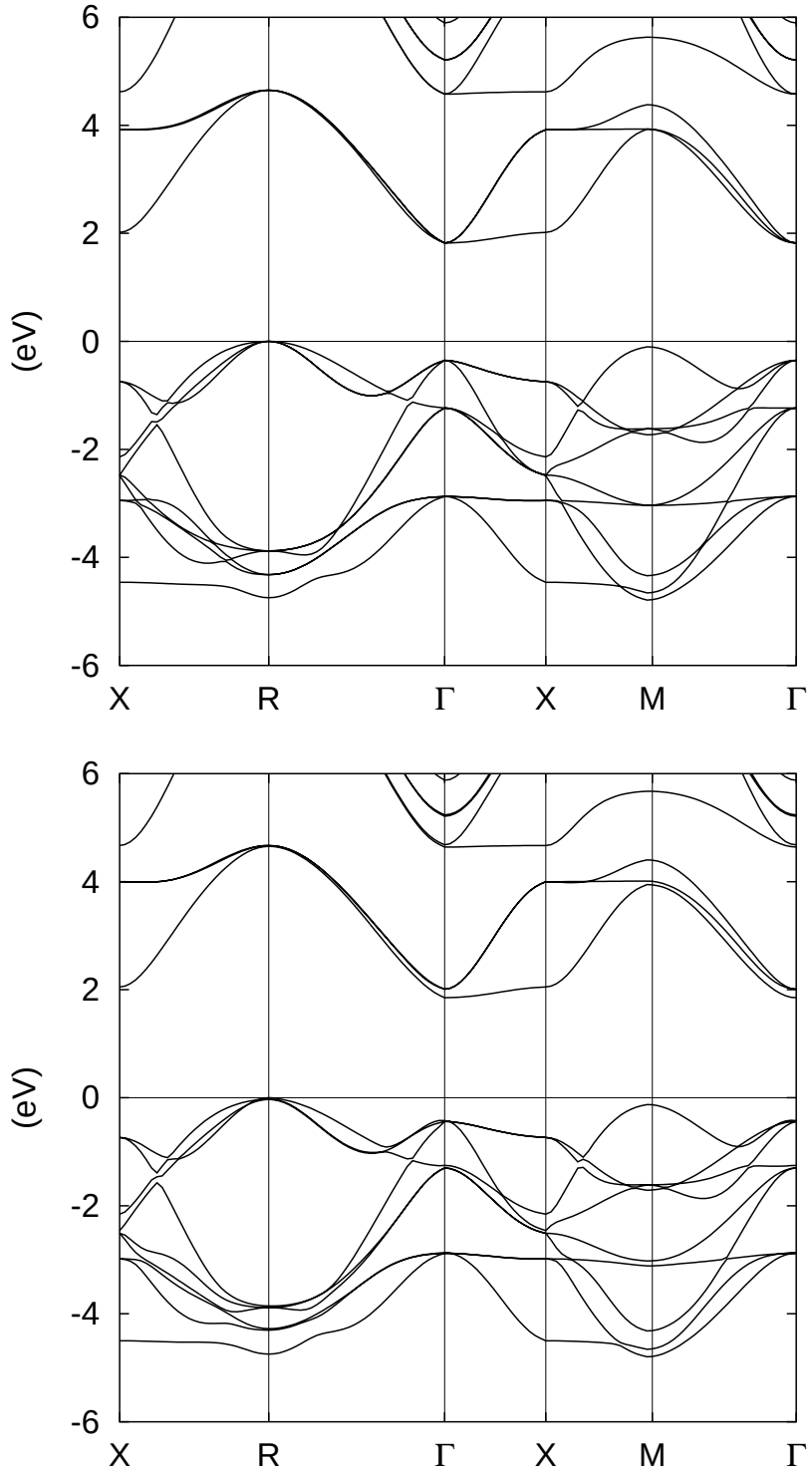

Figure 6.3: $SrTiO_3$ band structure. Upper panel: perfect cubic structure. Lower panel: ferroelectric-distorted structure (not AFD).

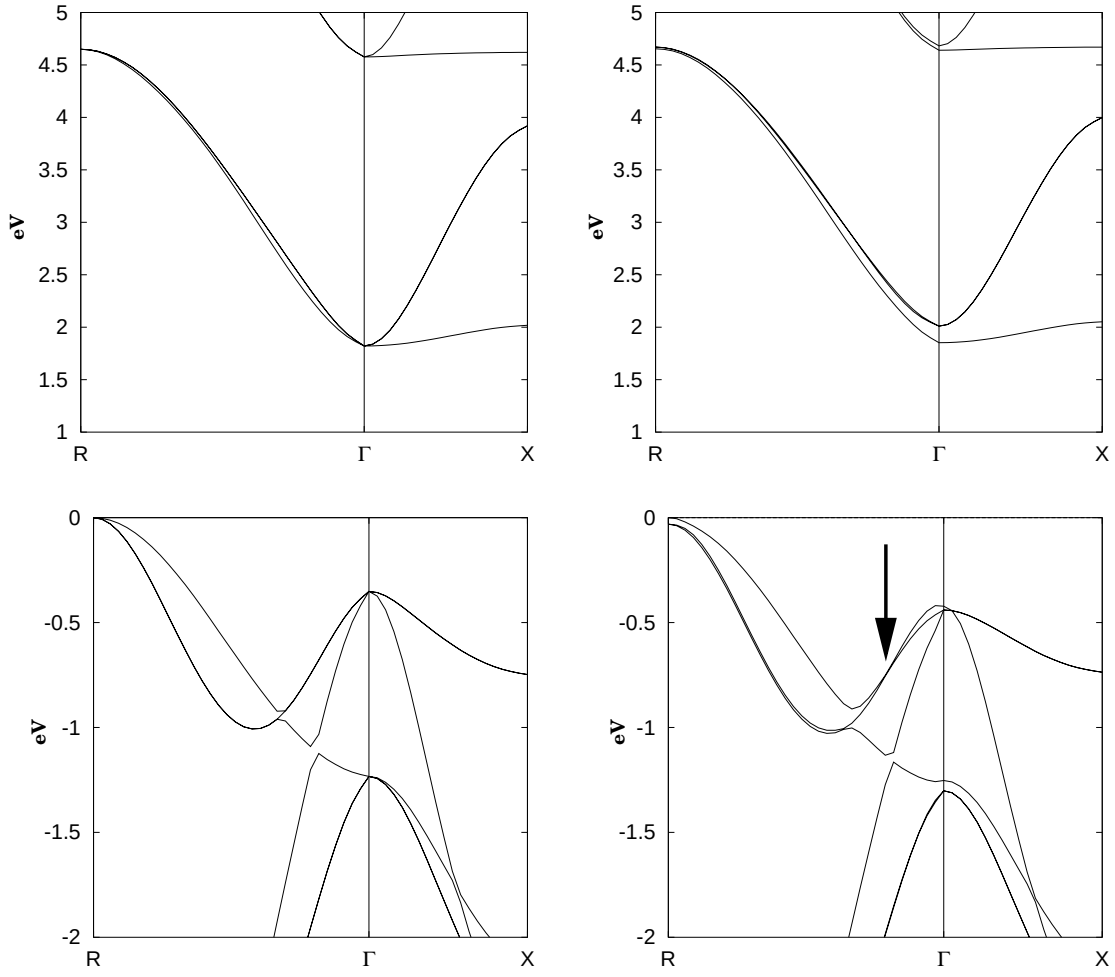

Figure 6.4: Detail of $SrTiO_3$ band structure, near Γ point. Left: cubic undistorted structure. Right: cubic ferroelectric-distorted structure. The top of the valence bands and the bottom of conduction bands are shown. The arrow mark δk, as discussed in the text.

6.3 Ferroelectricity of $KTaO_3$ under uniaxial stress

Starting with the ideal, classically stable paraelectric structure of $KTaO_3$, ferroelectricity can be driven along directions of lattice expansion by external strain [60]. We will do that theoretically in the following, with the aim of extracting constant energy surfaces, soft mode frequencies and eigenvectors of the zero temperature ferroelectric phase of $KTaO_3$.

In order to apply a uniaxial stress in the [001] direction, we compressed the lattice spacing in one direction, and by a series of total energy calculations, we minimized the total energy as a function of the lattice spacing in the [100] and [010].

Then we calculated the zone center phonons in the tetragonal structure. The T_{1u} mode in the cubic structure splits into a 2-fold degenerate E_1 mode and a non-degenerate A_1 mode.

The A_1 mode is polarized in the [001] direction and it is found to be stable (i.e. $\omega^2 > 0$) in all cases. Moreover, the frequency of the A_1 mode is harder than that of the T_{1u} mode, mirroring the fact that ferroelectricity is suppressed by pressure, as the TaO_6 cage shrinks in one direction. The E_1 mode is polarized in the perpendicular directions and it is found to be unstable, except for the smallest strain. These results are summarized in table 6.3.

The determination of the adiabatic trajectories of the nuclei on the potential energy surface, in principle would require a series of structural optimizations of all the internal coordinates; however, by using symmetry, the number of internal coordinates can be reduced to less than the cartesian coordinates of the system (3×5).

Moreover, if we combine the two E_1 modes with an phase angle θ, as for the pseudorotation of benzene, the amplitude $A(\theta)$ is the only quantity that needs to be minimized. We notice that the configurations that minimize the energy as a function of the amplitude ($\partial E/\partial A(\theta) = 0$), provides a very good

[001] **Strain**	**a (=b) (Å)**	**c/a**	$\omega(E_1)$ **(cm^{-1})**	$\omega(A_1)$ **(cm^{-1})**
1%	4.037	0.977	44	178
2%	4.063	0.960	$136i$	174
3%	4.077	0.947	$196i$	201

Table 6.3: Effect of a uniaxial stress on $KTaO_3$. Strain is referred to the relative compression of the c axis, relative to the experimental cubic lattice spacing. $\omega(E)$ and $\omega(A)$ are the frequencies of the ferroelectric mode perpendicular and parallel to the tetragonal axis.

starting point for the full structural optimization, as a function of the phase angle θ.

As an example, fig. 6.5 shows the total energy as a function of the amplitude $A(\theta)$, for a uniaxial stress of 3%. Table 6.4, for instance, shows the pattern of atomic displacement for $\theta = 0°$, in the minimum of $E[A(\theta)]$ and after the full relaxation of atomic positions. The relaxation took only few steps of structural minimization. This reflects the fact that the trajectory generated by combining the two eigenmodes is very close to the adiabatic trajectory. As an example, the two trajectories are compared in fig. 6.6 for an oxygen atom in the TaO_4 plane.

After having determined the atomic displacements for the three phase angles $0, \pi/8, \pi/4$, we assumed a simple rosette-like analytic form for the trajectory of each atom:

$$\begin{cases} x_l(\theta) = A_{x,l}(\theta)\cos(\theta) \\ y_l(\theta) = A_{y,l}(\theta)\sin(\theta) \\ A(\theta) = a + b\cos(4\theta) + c\cos(8\theta), \quad \theta \in [0, 2\pi), \end{cases} \tag{6.26}$$

and fitted the analytic expression on the calculated points.

The shape of the actual trajectory is shown in fig. 6.7 and in fig. 6.8. The potassium, the tantalum and the oxygen atoms not belonging to the TaO_4 plane, follow a highly symmetric trajectory, elongated in the [110] direction. Conversely, the two in-plane oxygen atoms follow a very anisotropic

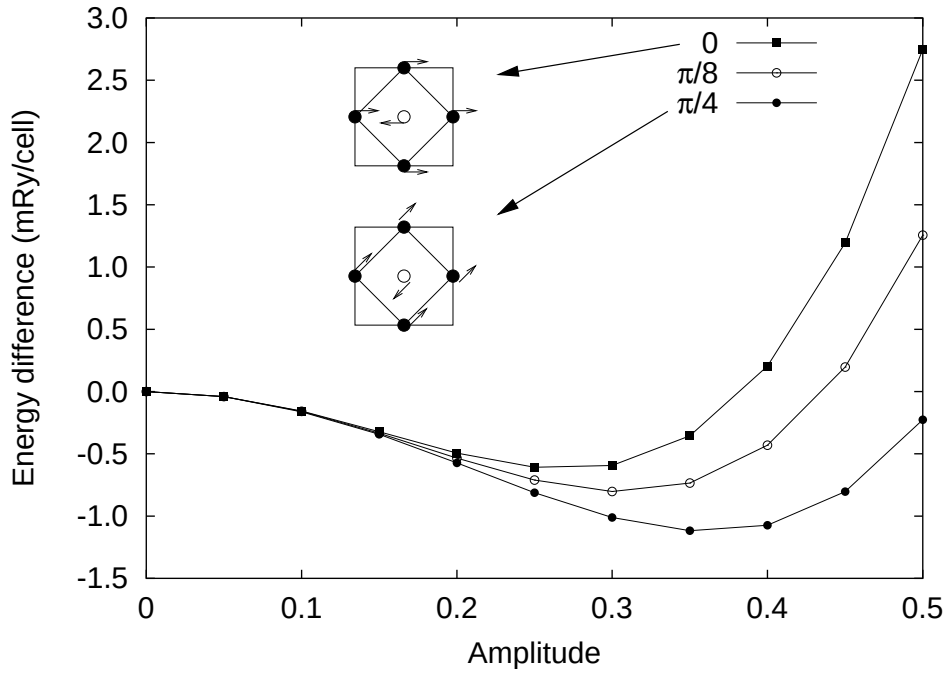

Figure 6.5: Energy as a function of the amplitude of the E_1 mode, for three phase angles θ. The results are for a uniaxial stress of 3%. Insets: polarization of the ferroelectric distortion; only the TaO_4 plane is shown, and Ta is in the center.

trajectory, elongated in the direction of the Ta–O bond. During the pseudorotation (fig. 6.8), the tantalum atom breaks one strong Ta–O bond ($\theta = 0$) and moves off-center, reaching the maximum elongation for $\theta = \pi/4$. In this configuration, also the two in-plane oxygens move to approach the tantalum atom, forming two weak Ta–O bonds. Although these two bonds are slightly weaker than the initial Ta–O bond, the system gains 18.50 meV/cell when the Ta atom is displaced in the [110] direction. The energy gain in the [100] direction is 10.06 meV/cell, which is approximately a factor 1/2. In fact the energy per bond is 9.25 meV/cell for the [110] direction.

For the less strained system (2%), the results are qualitatively the same, except that the system is less favorable to ferroelectricity. In fact the off-

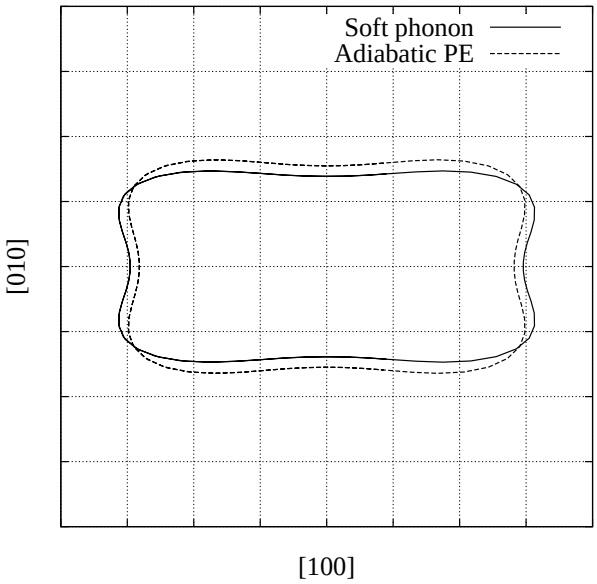

Figure 6.6: Comparison between the soft-mode trajectory and the adiabatic one for the oxygen in the TaO_4 plane (3% strain ferroelectric phase).

Atom	**Position**	E_1 **displacement**	**Fully relaxed**
K	(0, 0, 0)	0.0041	0.0079
Ta	(1/2, 1/2, 1/2)	−0.0059	−0.0070
O	(0, 1/2, 1/2)	0.0216	0.0206
O	(1/2, 0, 1/2)	0.0102	0.0113
O	(1/2, 1/2, 0)	0.0252	0.0280

Table 6.4: Displacement pattern in $KTaO_3$, strained by 3%. E_1 displacement is the eigenvector of the E_1 mode in [100] direction which minimizes total energy ($\Delta E = -8.30$ meV/cell). The fully relaxed structure is 10.06 meV/cell lower in energy relative to the undistorted configuration.

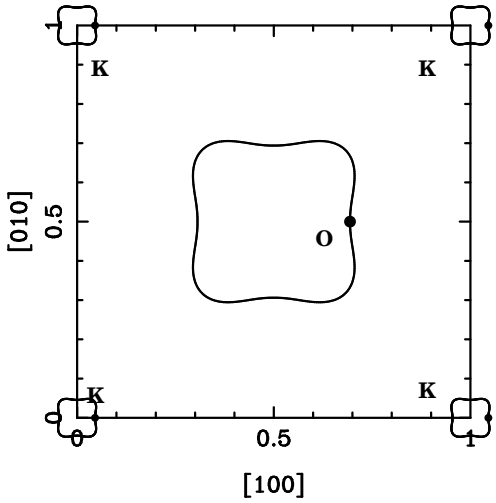

Figure 6.7: $KTaO_3$: adiabatic trajectory for the potassium (corner) and oxygen atoms (center), on the $z = 0$ plane (strain = 3%). All the atoms rotate in the same sense. The amplitude of the trajectory has been rescaled up by a factor 20.

center displacement of the atoms is smaller than for 3% strain, by a factor roughly 1/3. The maximum elongation of the Ta atom is again in the [110] direction, and the energy gain in this case is 0.54 meV/cell. The shape of the trajectory of the atoms on the TaO_4 is shown in fig. 6.9. Apart the smaller size, the orbits of the two oxygen atoms are less anisotropic, and the aspect ratio is $\simeq 0.6$, while for the more strained sample it was $\simeq 0.5$.

For the smallest strain (1%), the ferroelectric mode is now stable, and one cannot apply the same procedure. Nonetheless, we can now calculate the magnetic screening effect on the soft phonon. To this end, we let the atoms follow the trajectory generated by combining the E_1 eigenvectors, with a constant amplitude. Practical calculation is best done with a finite tantalum off-center displacement (we use here 0.04 Å). The resulting elliptical trajectories have an area intermediate between those calculated at 3% and 2% strain, and as expected they are similarly elongated in the [100] and [010] directions.

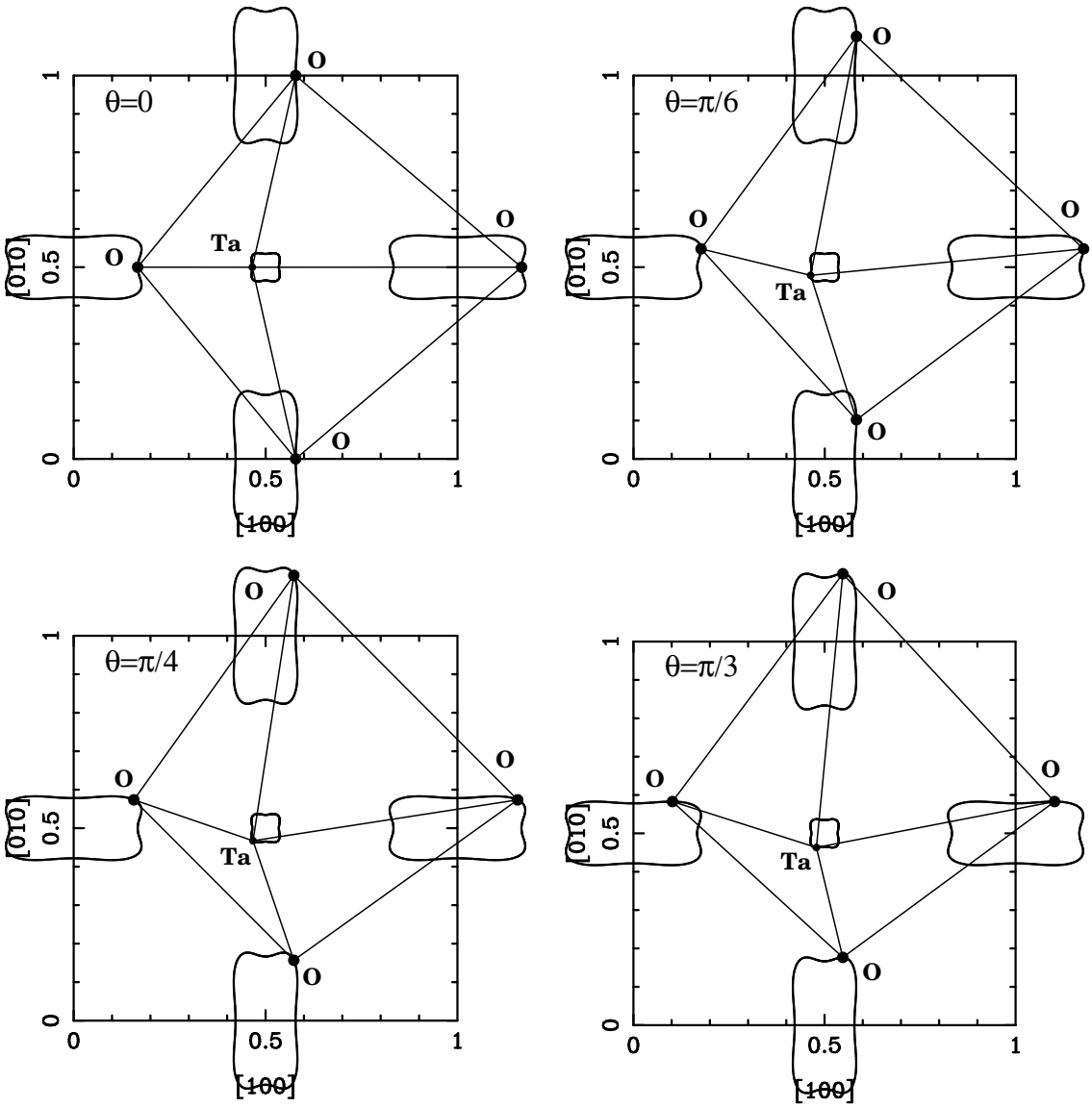

Figure 6.8: $KTaO_3$: adiabatic trajectory for the tantalum center and oxygen atoms, on the $z = 1/2$ plane (strain = 3%). All the atoms rotate in the same sense. The amplitude of the trajectory has been rescaled up by a factor 20. The Ta–O bond and O–O bonds are shown in the figure.

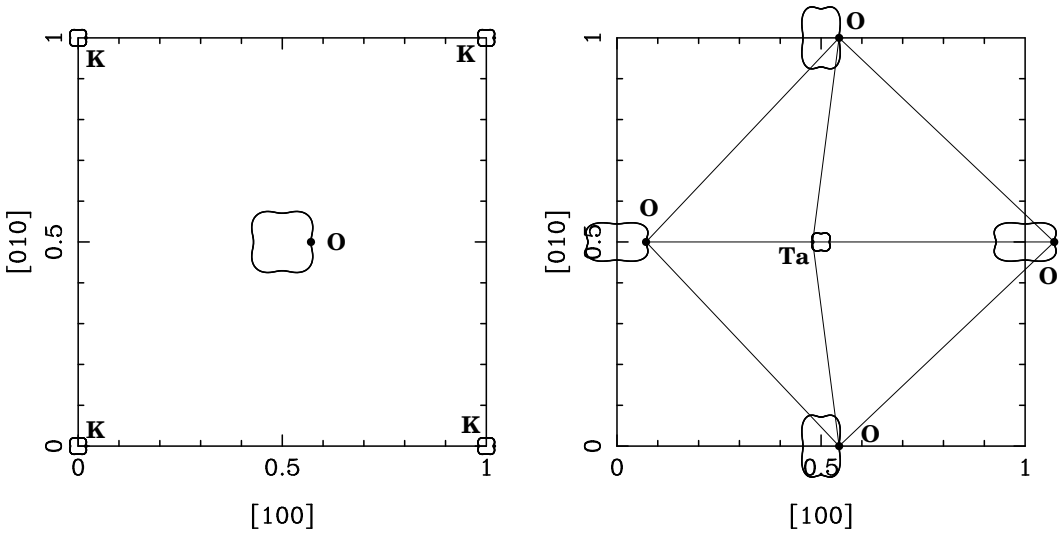

Figure 6.9: $KTaO_3$: adiabatic trajectory for the potassium, tantalum and oxygen atoms, (strain = 2%). The amplitude of the trajectory has been rescaled up by a factor 20. The Ta–O bond and O–O bonds are shown in the right panel.

6.4 Ferroelectricity in tetragonal $SrTiO_3$

At the experimental lattice spacing classical $SrTiO_3$ is, within our LDA calculations, unstable both to a zone center ferroelectric mode, and to a zone border antiferrodistortive (AFD) mode [61]. The cubic to AFD tetragonal $SrTiO_3$ consists in rotation of TiO_6 octahedra plus a small expansion of the lattice in the direction perpendicular to the AFD plane, and a small compression in the other two directions, relative to the cubic structure. The tetragonal structure is again unstable to two zone center ferroelectric modes $A_{2u} + E_{1u}$ coming from the threefold degenerate T_{1u} mode in the cubic symmetry.

We used the same lattice strain and internal coordinates as determined accurately by Sai and Vanderbilt [61], relatively to the cubic structure at the experimental lattice spacing. The TiO_6 octahedra are rotated by 4.93° (5° in experiment [75]) and the the tetragonal distortion is $c/a = 1.004$.

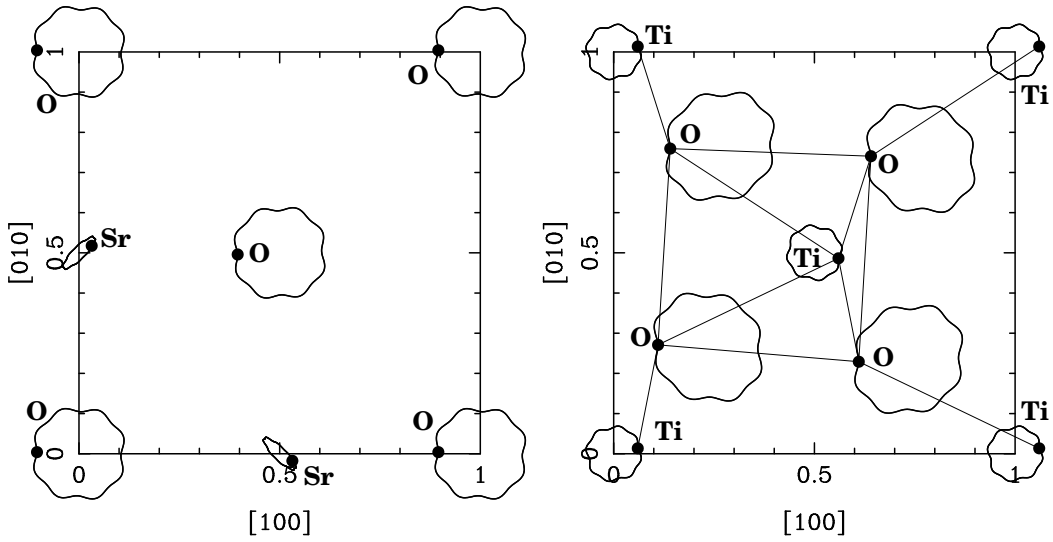

Figure 6.10: Adiabatic trajectory for the strontium, titanium and oxygen atoms, in the AFD distorted tetragonal structure of $SrTiO_3$. All the atoms rotate in the same sense. The amplitude of the trajectory has been rescaled up by a factor 20. The Ti–O bond and O–O bonds are shown in the right panel.

The calculated phonon frequencies and eigenvectors agree well with those reported by Sai and Vanderbilt [61]. The E_{1u} and A_{2u} modes are found to be unstable by, respectively, $\omega_E = 100i$ cm^{-1} and $\omega_A = 112i$ cm^{-1}, slightly more unstable than in the calculation of Sai ($\omega_E = 96i$ cm^{-1} and $\omega_A = 96i$ cm^{-1}), the difference probably due to parameters controlling the convergence of the calculations.

The calculated E_{1u} eigenvectors generate a pseudorotation in the (001) plane, perpendicular to the tetragonal axis. The adiabatic trajectories of the ions are shown in fig. 6.10. The strontium atoms rotate around their center on a small orbit, elongated in the [110] and [1$\bar{1}$0] directions. The oxygen atoms move on large orbits, slightly elongated in the direction of titanium atoms; compared to $KTaO_3$, where the oxygens elongate much more toward the tantalum atom, the oxygen orbits are more isotropic, or nearly circular.

6.5 Magnetic screening in $KTaO_3$ and $SrTiO_3$

After having determined the classical trajectory of the ions, we can calculate Berry's phase in a magnetic field B, within the soft mode theory and using the dynamical matrix in magnetic field. For $KTaO_3$ it is sufficient following the trajectories up to the phase angle of $\theta = \pi/2$, since all subsequent configurations can be obtained by simple rotations of the calculated arc. We covered the arc in increments on 5°. The tetragonal phase of $SrTiO_3$ is lower in symmetry, and we covered the full half loop from 0 to π, again in steps of 5°. The classical vector potential term is easily integrated analytically, by knowing the area of the loops.

With this, we calculated the bare g-factor (the contribution of the bare nuclei) using equation 6.15. The total g-factor can be finally obtained by the magnetic screening, as the total orbital magnetic moment is given by:

$$\mu_N g = \mu_{\text{bare}} + \mu_{\text{el}} = \mu_N g_{\text{bare}}(1 + \sigma). \tag{6.27}$$

The results are summarized in table 6.5. Notice that the calculated σ is negative and larger than one in modulus. This means that the electrons overscreen the orbital magnetic moment of the nuclei.

The oxygen atoms are negatively charged and move on large orbits, while the other ions (K and Ta; Sr and Ti) are positively charged but move on smaller orbits. As all the atoms rotate in the same sense, a cancellation of the magnetic moment must occur, but the contribution from the oxygen atoms is evidently stronger, and it overcomes the magnetic moment of the other ions. The net result is that the electronic current overscreen the nuclear currents in these ferroelectrics.

In order to clarify that further, we estimated what the pseudorotational g-factor would be if instead of the above, correct procedure, it was assumed simply that ions displaced their dynamical effective charge instead of the bare nuclear charges. Generally, in all perovskites the oxygen Born effective charge is anisotropic and the derivation of eq. 6.15 should be modified in order to take into account the full tensorial form of the Born charges. We

	state	g_{bare} (eq. 6.15)	σ	**g-factor**	$\mathbf{g}^\star$
$KTaO_3$ (strain 3%)	FE	0.2519	-1.316	-0.079	-0.176
$KTaO_3$ (strain 2%)	FE	0.2482	-1.709	-0.176	-0.169
$KTaO_3$ (strain 1%)	PE	0.2298	-1.667	-0.153	-0.163
$SrTiO_3$	FE	0.2267	-2.381	-0.313	-0.221

Table 6.5: Magnetic screening and g-factor in $KTaO_3$ and $SrTiO_3$. The bare g-factor accounts only for the magnetic moments of the bare nuclei. The total g-factor is negative, and the magnetic screening shows that electrons overscreen the magnetic orbital magnetic moment of nuclei. $g^\star$ is the g-factor calculated with eq. 6.15 and Born effective charges. FE means ferroelectric; PE means paraelectric.

know in fact that $Z_{Sr} = 2.56$, $Z_{Ti} = 7.26$, $Z_O(//) = -5.73$ and $Z_O(\perp) = -2.15$ from ref. [76] for $SrTiO_3$, and we calculated $Z_K = 0.79$, $Z_{Ta} = 8.49$, $Z_O(//) = -6.17$ and $Z_O(\perp) = -1.50$ for $KTaO_3$. To obtain as a rough estimate, we used 1/3 of the trace of the Born charge tensors and the results are denoted by $g^\star$ in table 6.5. The resulting g-factors are actually close to the calculated pseudorotational g-factors, especially for $KTaO_3$.

In conclusion, the pseudorotational g-factor on incipient ferroelectric perovskites is small and negative, and that is due to relatively large orbits of the oxygen atoms overscreening the opposite contribution of the cations.

Chapter 7

Dielectric response of ferroelectrics in a magnetic field

We now would like to investigate consequences of our results in chapter 6. One relevant question is: what will be the effect of magnetic field on the dielectric function of solids? Experimental data of Lawless and coworkers [19] show that the static dielectric constant of two incipient ferroelectric materials ($SrTiO_3$ and $KTaO_3$) depends quadratically on the applied magnetic field, increasing in the case of $SrTiO_3$ and decreasing in the case of $KTaO_3$ (fig 7.1). Other interesting systems are some high-dielectric constant glasses of the family of barium-oxide aluminum-oxide silica [9]. Those materials might be considered as incipient ferroelectrics; in fact they possess very low frequency modes and large correlation lengths on the scale of 20 Å. Remarkably, even a small magnetic field influences the dielectric constant, as shown in fig. 7.2. The dielectric response of an insulating solid can be expressed as:

$$\epsilon(\omega) = \epsilon_{\text{opt}}(\omega) \prod_i \frac{\omega^2 - \omega_{L,i}^2}{\omega^2 - \omega_{T,i}^2}, \tag{7.1}$$

where $\epsilon_{\text{opt}}(\omega)$ is the high-frequency optical dielectric function (equal to the square refractive index n^2 at lattice frequencies), $\omega_{L,i}$ and $\omega_{T,i}$ are the optical

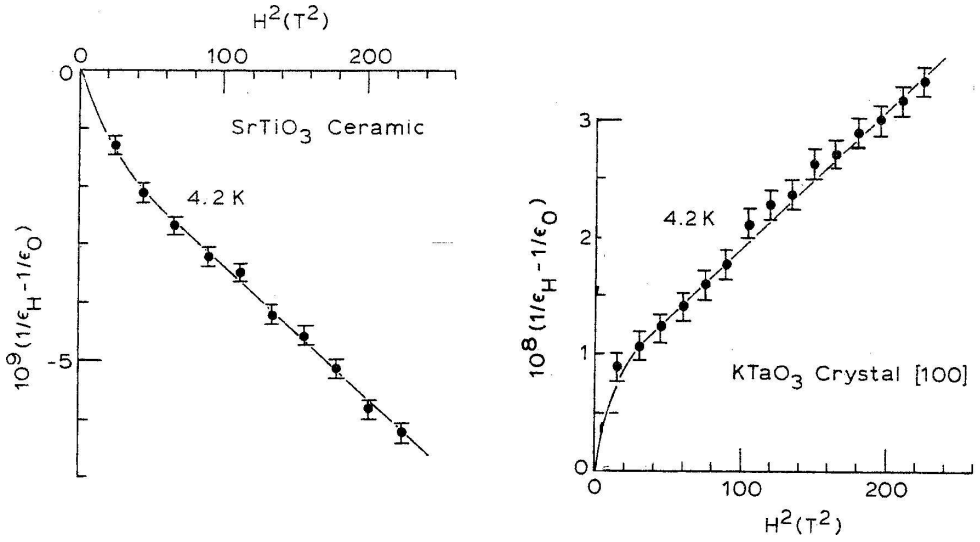

Figure 7.1: Magnetic field dependence of the dielectric constant in $KTaO_3$ and $SrTiO_3$, from Lawless [19].

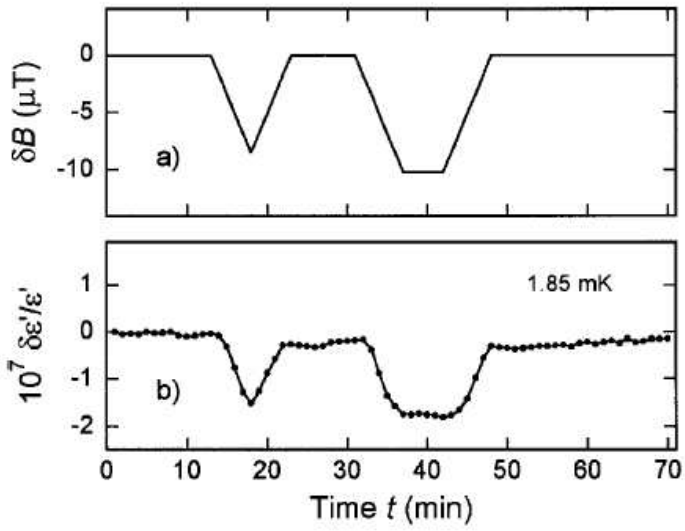

Figure 7.2: Influence of the magnetic field on the dielectric constant of some glasses. Upper panel: time variation of the applied magnetic field. Lower panel: relative change of the dielectric constant [9, 10, 11, 12].

active longitudinal and transverse mode frequencies. At zero frequency, the static version of eq. 7.1 is:

$$\epsilon_0 = \epsilon_\infty \prod_i \frac{\omega_{L,i}^2}{\omega_{T,i}^2}. \tag{7.2}$$

When a magnetic field is applied, several different effects can be envisaged:

(i) Valence and conduction bands turn into a multiplicity of Landau levels. In the simplest model, the minimum direct gap suffers a slight increase (fig. 7.3):

$$\Delta E_{\text{gap}} \simeq \frac{1}{2}\left(\hbar\omega_c^v + \hbar\omega_c^c\right), \tag{7.3}$$

and this will cause a slight field-induced decrease of refractive index, i.e. $\epsilon_\infty = \epsilon_\infty(B)$.

(ii) The Landau level quantization of bands will also provoke a change of screening (electron-phonon coupling) that can cause a change of phonon frequency, particularly of the soft mode $\omega_{T,0}$. This effect most likely results in an increase of $\omega_{T,0}$, and therefore also reduces $\epsilon_0(B)$.

(iii) The soft mode, being a rotor involving charges, couples to the magnetic field through the orbital g-factor of chapter 6, leading to magnetic field-induced shift and splitting of optically active modes, which changes the dielectric response.

Of these effects, the first two (i) and (ii) appear to depress ϵ_0, while the latter (ii) can increase ϵ_0, because one of the split soft modes can drop in frequency. Only the second effect (ii), i.e. the soft mode shift due to Landau band quantization via electron-phonon coupling appear to have been considered earlier by Bersuker and collaborators [6, 5, 7].

In this thesis, we will concentrate on only an effect that can lead to an enhancement of ϵ_0, namely the direct field-rotor coupling (iii).

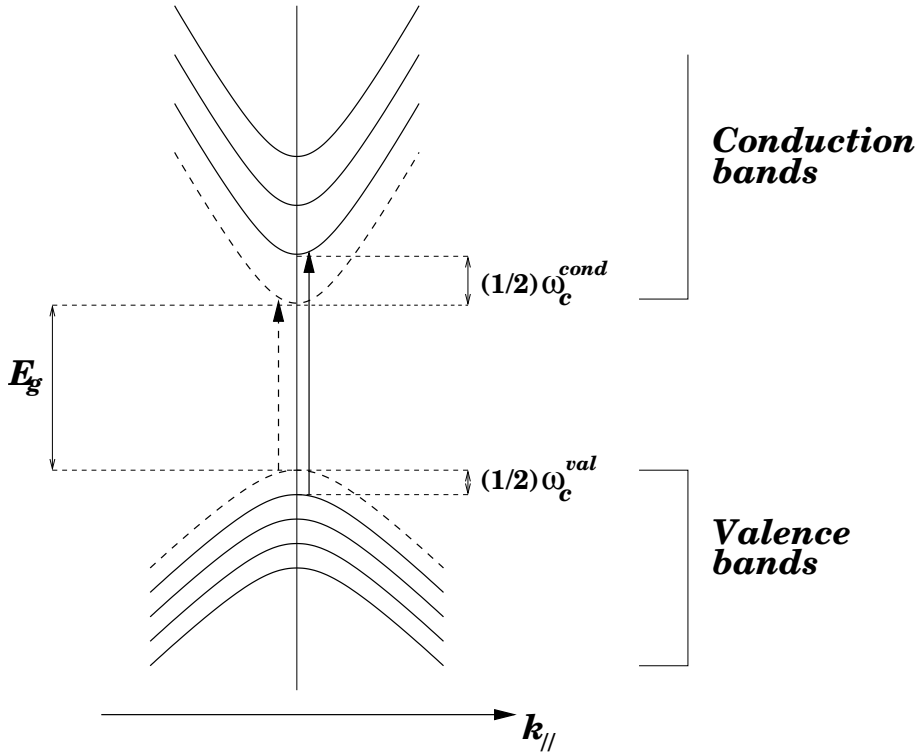

Figure 7.3: Magnetic field effect on the optical transitions. The original valence and conduction bands (dashed lines) are substituted by Landau levels (full lines). The offset of the first Landau level respect to the original bands are half the cyclotron mass for the electrons and for the holes.

7.1 Estimate of dielectric function change in magnetic field

Ignoring all effects except (iii) above, the static dielectric function may be written as:

$$\frac{\epsilon_0(B)}{\epsilon_\infty(B)} = \text{const.} \times \sum_i \frac{f_i}{\omega_i^2}, \tag{7.4}$$

where the sum runs over the threefold degenerate soft mode, f_i is the oscillator strength, ω_i is the frequency and the constant is the contribution of order 1, of all other optically active modes of higher frequency.

Except perhaps very close to the ferroelectric-paraelectric transition, the large value of ϵ_0 found in displacive ferroelectrics is almost entirely determined by the low soft-mode frequency. As ω_0 goes to zero, the dielectric constant diverges.

The effect of magnetic field on the static dielectric constant is to split the degenerate T_1 mode, and the calculation must take into account the new transitions energies and the change in the oscillator strengths, as a function of the applied magnetic field.

At the beginning of chapter 6, we calculated the dynamical matrix in magnetic field and obtained the soft mode splitting like an orbital Zeeman interaction:

$$\Delta\omega = 0, \pm\mu_N g B. \tag{7.5}$$

Within the classical theory, the oscillator strengths are given by the electric dipoles, which are to lowest order unchanged by the magnetic field. Of the three original T_{1u} modes, the one polarized parallel to the magnetic field is unaffected, whence, the zero frequency dielectric response parallel to the magnetic field is independent from the magnetic field (fig 7.4):

$$\epsilon_{//}(B) = \epsilon_0|_{B=0}\,. \tag{7.6}$$

Conversely, the static dielectric response in the direction perpendicular to

the magnetic field, is:

$$\frac{\epsilon_0(B)}{\epsilon_\infty} \propto \frac{1}{2}\left[\frac{f}{(\omega_0+\Delta\omega)^2}+\frac{f}{(\omega_0-\Delta\omega)^2}\right] \tag{7.7}$$

$$\simeq \frac{\epsilon_0(B=0)}{\epsilon_\infty}\left[1+3\left(\frac{\Delta\omega}{\omega_0}\right)^2\right]. \tag{7.8}$$

In deriving this result, we have assumed $\Delta\omega \ll \omega_0$ and we expanded in powers of $\Delta\omega/\omega_0$. Notice that the terms linear in $\Delta\omega$ cancel; if on the other hand, the soft mode frequency becomes very small, of the order of $\Delta\omega$, this expansion is no more valid, and the relative change of dielectric constant will diverge as ω_0 approaches zero.

The dielectric constant is expected always to *increase* as an effect of an external magnetic field. Within linear theory, the increase is thus:

$$\frac{\Delta\epsilon_\perp}{\epsilon_0} = 3\left(\frac{\Delta\omega}{\omega_0}\right)^2. \tag{7.9}$$

7.2 Dielectric function change for $KTaO_3$ and $SrTiO_3$

Now we come to the actual case of $KTaO_3$ and $SrTiO_3$. From the theory of the dynamical matrix in a magnetic field we have calculated the total (ionic + electronic) the bare ionic orbital magnetic moment and the bare g-factor (eq. 6.15). Then, we calculated the magnetic screening for orbital motion of the ions, and the total pseudorotational g-factor.

Using the g-factor calculated at the end of the previous chapter, being $\mu_N B = 2.54\cdot 10^{-4}\ \mathrm{cm}^{-1}(B/\mathrm{Tesla})$, and using equation 7.9:

$$\Delta\epsilon_\perp/\epsilon_0 = 3\frac{g^2(\mu_N B)^2}{\omega_0^2}, \tag{7.10}$$

$$KTaO_3 : \Delta\epsilon_\perp/\epsilon_0 \simeq +1.4\cdot 10^{-9} \quad (B = 10\ \mathrm{Tesla},\ \omega_0 = 21\ \mathrm{cm}^{-1}), \tag{7.11}$$

$$SrTiO_3 : \Delta\epsilon_\perp/\epsilon_0 \simeq +7.1\cdot 10^{-10} \quad (B = 10\ \mathrm{Tesla},\ \omega_0 = 16\ \mathrm{cm}^{-1}). \tag{7.12}$$

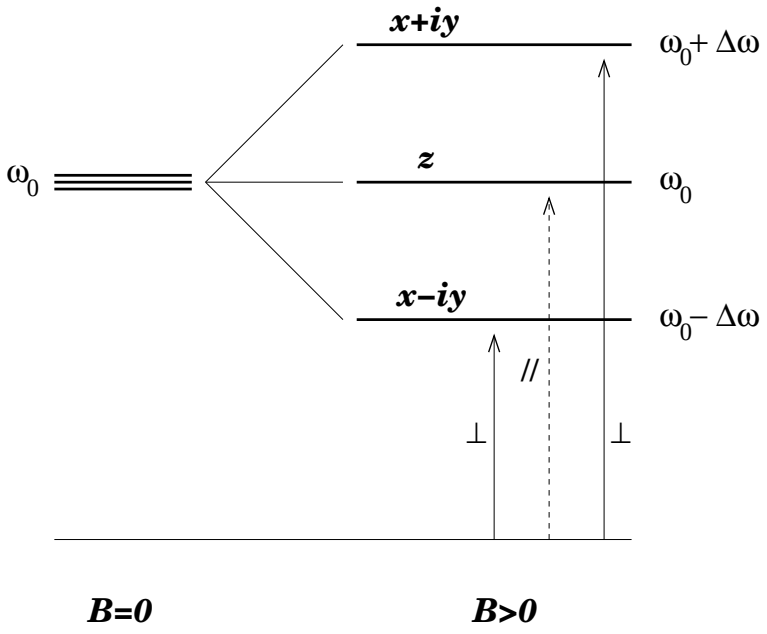

Figure 7.4: Magnetic field-induced splitting of the soft mode. $\Delta\omega$ is proportional to the magnetic moment. The pattern of splitting is the same of the Zeeman splitting on an $L = 1$ state. The transitions contributing to the dielectric response are represented by vertical lines. $\perp$ is the dielectric response perpendicular to the magnetic field. // is the parallel one.

From the work of Lawless and coworkers (see fig. 7.1), the relative variation of dielectric constant can be extracted (in their samples of $KTaO_3$ and $SrTiO_3$ the dielectric constants were 3772 and 6088 respectively):

$$KTaO_3 : \Delta\epsilon_0/\epsilon_0 \simeq -7.5 \cdot 10^{-5} \quad (B = 10 \text{ Tesla}), \tag{7.13}$$

$$SrTiO_3 : \Delta\epsilon_0/\epsilon_0 \simeq +1.8 \cdot 10^{-5} \quad (B = 10 \text{ Tesla}). \tag{7.14}$$

The calculated values are four order of magnitude less than the experimental data, and always predict an increase of dielectric constant. We didn't find in literature any later experimental data to compare to, measured after the work of Lawless [19]. This work came at the end of a sequel of experimental data, often showing discrepancies and contrasts among them [77, 78, 79, 80, 81], probably due to the difficulty of these low temperature measurements. We must conclude that at least within our mean-field theory, the orbital Zeeman coupling of the soft mode is unable to account for the reported magnetic field dependence of the dielectric constant of $KTaO_3$ and $SrTiO_3$.

Chapter 8

Conclusions

In this work, we have considered the magnetic screening of the electrons on the nuclei by the geometric vector potential and we have established a clear link between the Berry phase and the total (nuclear + electronic) orbital magnetic moment, in molecules and solids.

We have developed and tested two techniques for calculating the magnetic screening both in isolated molecules and periodic solids. Both two techniques (plane waves and localized basis set), are based on a Berry phase formulation, giving the electronic contribution to the orbital magnetic moment. Like the macroscopic polarization in insulators, which is not determined by the sole knowledge of the charge density distribution, also in our case the orbital magnetic moment in not determined by the charge density but rather by the geometric phase acquired in the magnetic field by the electronic wavefunction after a closed loop in the configuration space spanned by the nuclear coordinates.

The localized basis method we have developed, helps understanding that: for instance, for the hydrogen molecule, the Berry's phase is totally accounted by the Peierls' phase between the two $1s$ orbitals. Moreover, if one treats the electron distribution in H_2 as if it were a classical rotating charge distribution, its orbital magnetic moment would overscreen enormously that of the bare nuclei ($g_{\text{classic}} = -0.79$). The reason for that is that the electron charge

density extends in far out regions of space, and the expectation value of r^2 is much larger than the square R^2 of the proton-proton bond length. Both the plane wave and the localized basis methods reproduce well the experimental g-factor of some molecules and also compare well with existing quantum chemical calculations, which, on the other hand, cannot easily extended to periodic systems.

Next, we applied our technique to solids, as the codes are ideally suited for treating periodic systems. We studied pseudorotations represented by soft modes in perovskites. They should be accompanied by an orbital magnetic moment, interacting with an external magnetic field via an orbital Zeeman coupling. The main result of our calculations is *overscreening* of the nuclear orbital magnetic moment in the perovskites. The dominating contribution is due to oxygen atoms, which carry around electrons on large orbits, compared to the other ions. This remarkable result is also supported by an estimate done with Born effective charges (see tab. 6.5).

The calculated total orbital magnetic moments, together with the theory of the dynamical matrix in a magnetic field, allows us to calculate the orbital Zeeman effect of the magnetic field on the soft ferroelectric modes. As discussed in the previous chapter, there are several effects that lead to a magnetic field dependence of the dielectric constant. From the Lyddane-Sachs-Teller relation:

$$\epsilon_0(B) = \epsilon_\infty(B) \prod_i \frac{\omega_{L,i}^2}{\omega_{T,i}(B)^2}, \tag{8.1}$$

where ϵ_∞ is the optical dielectric constant, $\omega_{L,i}$ and $\omega_{T,i}$ are the frequencies of the longitudinal and transversal optic modes.

In this work we considered only the variation and splitting of ω_T due to the orbital Zeeman effect. The estimated increase of the static dielectric constant $\epsilon_0(B)$ is moreover much smaller than the experimental value (and even of opposite sign in the case of $KTaO_3$). The orbital Zeeman effect, probably, is not the dominant effect. The influence of the magnetic field on the electronic structure could be much more significative than the effect on

the lattice. However, there is no simple effect that will explain the large increase seen in $SrTiO_3$ [19].

The relative change in dielectric constant (eq. 7.9) will increase as the soft-mode frequency (ω_0) approaches to zero. For this reason, we suggest that this effect could be detectable when the system is driven toward ferroelectricity, i.e. by applying pressure. Then, at the Curie temperature, the dielectric should grow to be extremely large, an outright divergence suppressed by non-homogeneity of the samples. Measurements taken close to T_c (i.e. obtained by pressure) could detect precisely this effects.

In conclusion we have developed a technique for calculating the orbital magnetic moments and the g-factors for rotations and pseudorotations; our technique is based on the calculation of the electronic Berry phase in a magnetic field. Our calculated rotational g-factors compare very well with existing experimental data on simple molecules. The calculated pseudorotational g-factors for two incipient ferroelectric perovskites, even if they cannot be compared directly to experimental data, indicates that in general the oxygen atoms dominates the pseudorotational g-factor and they overscreen the nuclear orbital magnetic moments.

Appendix A

Estimate of dielectric function change in magnetic field in the spherical rotor model

In chapter 7, we have derived the magnetic field dependence of the dielectric constant, from the classical theory of the dynamical matrix in magnetic field. In earlier chapters, we have pointed out that the threefold degenerate T_{1u} mode correspond to the transition from the $L = 0$ state to the $L = 1$ state of a quantum spherical rigid rotor. In this section, we will estimate the magnetic field-induced dielectric function change, for the spherical quantum rotor. The unperturbed hamiltonian is:

$$\mathcal{H} = \frac{L^2}{2I}, \tag{A.1}$$

where $I = MR^2$ is the moment of inertia associated with the rotor. The energy separation between the $L = 0$ ground state and the $L = 1$ excited state is $\omega_0 = 1/I$.

The magnetic field acts like a perturbation, comprising a paramagnetic term and a diamagnetic term, both to be evaluated to first order:

$$\Delta\mathcal{H} = \frac{eB}{2Mc}L_z + \frac{e^2B^2}{8Mc^2}R^2\left(x^2 + y^2\right), \tag{A.2}$$

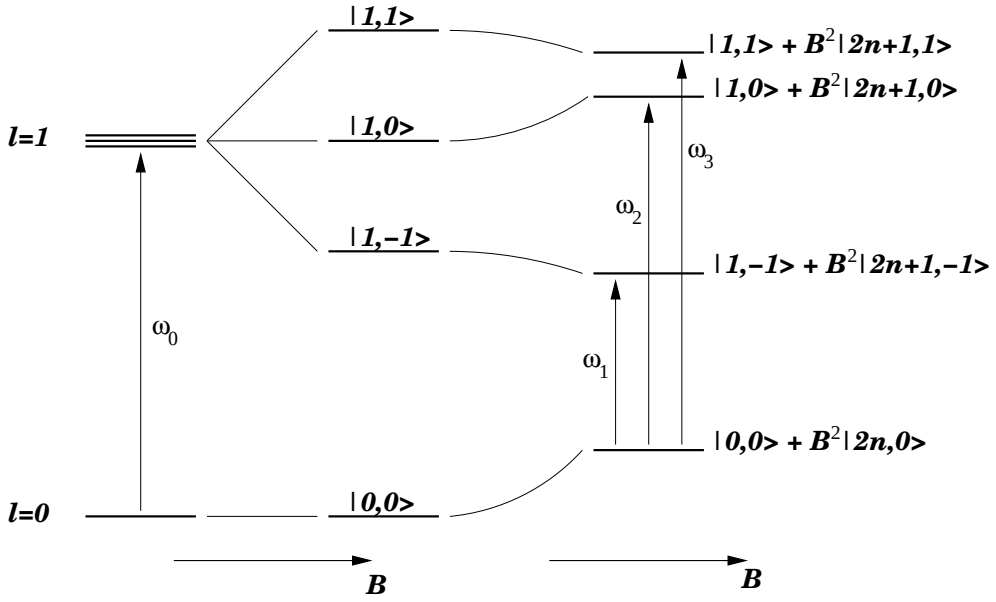

Figure A.1: Effect of the magnetic field on the energy levels and transitions in the rigid rotor. $l = 0$ represents the ground state and $l = 1$ represents the soft T_{1u} ferroelectric mode. The paramagnetic term splits the $|1, \pm 1\rangle$ states linearly in the magnetic field. The diamagnetic term always shifts the energy levels quadratically in the magnetic field, and it couples the $|l, m\rangle$ state with the $|l + 2k, m\rangle$ excited states, where k is a positive integer.

where we have taken $\mathbf{B} = (0, 0, B)$. Notice that the diamagnetic term depend on the radius of the rotor and it can be rewritten as:

$$\frac{e^2 B^2}{8M^2c^2} I\left(x^2 + y^2\right) = \left[\frac{eB}{2Mc}\right]^2 \frac{x^2 + y^2}{2\omega_0}. \tag{A.3}$$

The $L = 0$ and $L = 1$ levels are perturbed by the magnetic field as shown in fig. A.1. Notice that the paramagnetic term is diagonal in our representation, and splits the $L = 1$ state. The diamagnetic term shifts up the $|0, 0\rangle$ and the $|1, 0\rangle$ states and the opposite for the $|1, \pm 1\rangle$ states.
The new transition energies are:

$$\omega_1 \simeq \omega_0 - \mu B - \frac{17}{15}\frac{\mu^2 B^2}{\omega_0}, \tag{A.4}$$

$$\omega_2 \simeq \omega_0 - \frac{2}{15}\frac{\mu^2 B^2}{\omega_0}, \tag{A.5}$$

$$\omega_3 \simeq \omega_0 + \mu B - \frac{17}{15}\frac{\mu^2 B^2}{\omega_0}, \tag{A.6}$$

where $\mu = e/(2Mc)$ is the effective magneton of the rigid rotor, equal to the magnetic orbital moment we calculated in chapter 6.

Now, for an electric field parallel to magnetic field, the only allowed transition is ω_2 and the new oscillator strength changes to second order in the magnetic field (the diamagnetic term couples the $|l, m\rangle$ state with the states for which $\Delta l = 2, 4, 6, ...$, $\Delta m = 0$):

$$f_2 \simeq \left| 0.577 - 0.051\frac{\mu^2 B^2}{2\omega_0^2} \right|^2, \tag{A.7}$$

leading to an overall *increase* of the dielectric constant, quadratic in the magnetic field:

$$\frac{\Delta\epsilon_{//}}{\epsilon_0} \simeq 0.222\frac{\mu^2 B^2}{\omega_0^2}. \tag{A.8}$$

Conversely, if the electric field is perpendicular to the magnetic field, the only allowed transitions are ω_1 and ω_3:

$$f_{1,3} \simeq \left| 0.408 + 0.018\frac{\mu^2 B^2}{2\omega_0^2} \right|^2; \tag{A.9}$$

notice that in this case the two terms linear in the magnetic field ($\pm\mu B$) cancel and the final result is now a much larger again *increase* of the dielectric constant:

$$\frac{\Delta\epsilon_{\perp}}{\epsilon_0} \simeq 4.17\frac{\mu^2 B^2}{\omega_0^2}. \tag{A.10}$$

Also this model predicts that the static dielectric constant would always *increase* as a result of applying a magnetic field. In this case, in addition to the Zeeman splitting, the diamagnetic term shifts the transitions to higher frequencies. The dielectric response parallel to the magnetic field, is smaller than the perpendicular response, and it is determined by the diamagnetic interaction.

The change of the oscillator strengths is due to the diamagnetic coupling with excited states. The diamagnetic interaction contributes also the perpendicular dielectric response, as can be seen comparing eq. 7.9 and eq. A.10; the difference between the two formulas is the prefactor multiplying $(\Delta\omega/\omega_0)^2$; the diamagnetic interaction accounts for a factor $4.17/3 \simeq 1.4$, with respect to the derivation based on the dynamical matrix.

Furthermore, carrying out the same calculations considering a finite broadening of the transitions, the change in dielectric constant is slightly affected by a multiplicative factor $1 - (\delta\omega/\omega_0\pi)$, where $\delta\omega$ is the line width.

Acknowledgments

I would like to warmly thank Erio Tosatti, firstly for giving me the opportunity of working on very interesting and fascinating topics. Secondly, and more important, for having transmitted me his enthusiasm and a large part of his wisdom and knowledge of physics.

I want also thank Ugo, Matteo, Davide Marenduzzo, Giuseppe Santoro and Sandro Scandolo for useful discussions and Stefano de Gironcoli and Andrea Dal Corso, for technical advices. I thank again Prof. David Vanderbilt, for his pseudopotentials.

Finally, I would like to greet all my colleagues and friends I've met during this period in Sissa: Matteo, Davide, Luca, Giuliano, Evgeni, Oleg, Mahdi, Paola and Alessio; Ugo, Nicola, Fabien; all the new and old students; Giancarlo and two Francesco's.

Bibliography

[1] W. H. Flygare, Chem. Rev. **74**, 653 (1974).

[2] N. F. Ramsey, Phys. Rev. **58**, 226 (1940).

[3] L. A. Cohen, J. H. Martin, and N. F. Ramsey, Phys. Rev. A **19**, 433 (1979).

[4] E. Tosatti, N. Manini, and O. Gunnarsson, Phys. Rev. B **54**, 17184 (1996).

[5] I. B. Bersuker and B. G. Vekhter, Ferroelectrics **19**, 137 (1978).

[6] I. B. Bersuker, B. G. Vekhter, and V. P. Zenchenko, Ferroelectrics **13**, 373 (1976).

[7] B. G. Vekhter, V. P. Zenchenko, and I. B. Bersuker, Ferroelectrics **20**, 163 (1978).

[8] K. A. Müller and H. Burkard, Phys. Rev. B **19**, 3593 (1979).

[9] P. Strehlow, C. Enss, and S. Hunklinger, Phys. Rev. Lett. **80**, 5361 (1998).

[10] S. Kettemann, P. Fulde, and P. Strehlow, Phys. Rev. Lett. **83**, 4325 (99).

[11] P. Strehlow *et al.*, Phys. Rev. Lett. **84**, 1938 (2000).

[12] J. Le Cochec, F. Ladieu, and P. Pari, cond-mat/0203564 (2002).

[13] J. Gauss, K. Ruud, and T. Helgaker, J. Chem. Phys. **105**, 2804 (1996).

[14] S. M. Cybulski and D. M. Bishop, J. Chem. Phys. **100**, 2019 (1994).

[15] M. V. Berry, Proc. R. Soc. London A **392**, 45 (1984).

[16] C. A. Mead, Rev. Mod. Phys. **64**, 51 (1992).

[17] L. Yin and C. A. Mead, J. Chem. Phys. **100**, 8125 (1994).

[18] R. Resta, J. Phys. Cond. Mat. **12**, R107 (2000).

[19] W. N. Lawless, C. F. Clark, and S. L. Swartz, J. Phys. Soc. Japan **38**, 183 (1975).

[20] P. Hohenberg and W. Kohn, Phys. Rev. **136B**, 864 (1964).

[21] S. Baroni, S. de Gironcoli, A. Dal Corso, and P. Giannozzi, Rev. Mod. Phys. **73**, 515 (2002).

[22] W. Kohn and L. J. Sham, Phys. Rev. **140A**, 1133 (1965).

[23] J. P. Perdew and A. Zunger, Phys. Rev. B **23**, 5048 (1981).

[24] D. Sebastiani and M. Parrinello, J. Phys. Chem. **105**, 1951 (2001).

[25] R. Resta, Phys. Rev. Lett. **9**, 1800 (1998).

[26] N. Marzari and D. H. Vanderbil, Phys. Rev. B **56**, 12847 (1997).

[27] F. Mauri and S. G. Louie, Phys. Rev. Lett. **76**, 4246 (1996).

[28] F. Mauri, B. G. Pfrommer, and S. G. Louie, Phys. Rev. Lett. **77**, 5300 (1996).

[29] K. Ohno, F. Mauri, and S. G. Louie, Phys. Rev. B **56**, 1009 (1997).

[30] B. G. Pfrommer, Ph.D. thesis, Univ. of California at Berkeley, 1998.

[31] T. Gregor, F. Mauri, and R. Car, J. Chem. Phys. **111**, 1815 (1999).

[32] C. J. Pickard and F. Mauri, Phys. Rev. B **63**, 245101 (2001).

[33] H. von Busch *et al.*, Phys. Rev. Lett. **81**, 4584 (1998).

[34] A. Auerbach, N. Manini, and E. Tosatti, Phys. Rev. B **49**, 12998 (1994).

[35] N. Manini, E. Tosatti, and A. Auerbach, Phys. Rev. B **49**, 13008 (1994).

[36] R. D. King-Smith and D. Vanderbilt, Phys. Rev. B **47**, 1651 (1993).

[37] Q. Niu *et al.*, Phys. Rev. Lett. **83**, 207 (1999).

[38] J. C. Slater, *Quantum theory of molecules and solids* (McGraw-Hill, New York, 1963), Vol. 1.

[39] W. N. Cottingham and N. Hassan, J. Phys. B **23**, 323 (1990).

[40] S. M. Cybulski and D. M. Bishop, J. Chem. Phys. **106**, 4082 (1997).

[41] J. Peternelj, A. Damyanovich, and M. M. Pintar, Phys. Rev. B **49**, 3322 (1994).

[42] M. V. Berry, J. Chem. Phys. **33**, 933 (1960).

[43] N. Manini, Ph.D. thesis, SISSA/ISAS, 1995.

[44] G. Herzberg, *Molecular Spectra and Molecular Structure* (Van Nostand, New York, 1945), Vol. 2.

[45] J. P. Pinan *et al.*, J. Chem. Phys. **109**, 5469 (1998).

[46] D. Sanchez-Portal, P. Ordejon, E. Artacho, and J. M. Soler, Int. J. Quantum. Chem. **65**, 453 (1997).

[47] P. Ordejon, Phys. Stat. Sol. B **217**, 335 (2000).

[48] O. F. Sankey and D. J. Niklewski, Phys. Rev. B **40**, 3979 (1989).

[49] J. M. Luttinger, Phys. Rev. **84**, 814 (1951).

[50] K. A. Müller, W. Berlinger, and E. Tosatti, Z. Phys. B **84**, 277 (1991).

[51] E. Tosatti and R. Martoňák, Sol. State Comm. **92**, 167 (1994).

[52] C. Kittel, *Introduction to solid state physics* (Wiley, New York, 1976).

[53] R. Martoňák and E. Tosatti, Phys. Rev. B **49**, 12596 (1994).

[54] R. Martoňák and E. Tosatti, Phys. Rev. B **54**, 15714 (1996).

[55] S. Koval, J. Kohanoff, and R. L. Migoni, Ferroelectrics **268**, 659 (2002).

[56] L. Arzel *et al.*, Ferroelectrics **267**, 317 (2002).

[57] S. Rod, F.Borsa, and J. J. van der Klink, Phys. Rev. B **38**, 2267 (1988).

[58] S. Rod, Ph.D. thesis, Ecole polytechnique féderale de Lausanne, 1991.

[59] R. Blinc, J. Chem. Phys. Solids **13**, 204 (1960).

[60] H. Uwe and T. Sakudo, J. Phys. Soc. Japan **38**, 183 (1975).

[61] N. Sai and D. Vanderbilt, Phys. Rev. B **62**, 13942 (2000).

[62] N. Troullier and J. M. Martins, Phys. Rev. B **43**, 1993 (1991).

[63] J. M. Martins and N. Troullier, Phys. Rev. B **46**, 1766 (1992).

[64] C. J. Wu, L. H. Yang, J. E. Klepsis, and C. Mailhiot, Phys. Rev. B **52**, 11784 (1995).

[65] H. J. Monkhorst and J. D. Pack, Phys. Rev. B **13**, 5188 (1976).

[66] A. V. Postnikov, T. Neumann, G. Borstel, and M. Methfessel, Phys. Rev. B **48**, 5910 (1993).

[67] A. V. Postnikov, T. Neumann, and G. Borstel, cond-mat/9404083 (1994).

[68] A. V. Postnikov, T. Neumann, and G. Borstel, Ferroelectrics **164**, 101 (1995).

[69] D. J. Singh, Phys. Rev. B **53**, 176 (1996).

[70] C. H. Perry and T. F. McNelly, Phys. Rev. **154**, 154 (1967).

[71] R. D. King-Smith and D. Vanderbilt, Phys. Rev. **49**, 5828 (1994).

[72] A. García and D. Vanderbilt, Phys. Rev. B **54**, 3817 (1996).

[73] C. Lasota, C. Z. Wang, R. Yu, and H. Krakauer, Ferroelectrics **194**, 109 (1994).

[74] D. Vanderbilt, Phys. Rev. B **41**, 7892 (1990).

[75] K. A. Müller, W. Berlinger, and J. C. Slonczewski, Phys. Rev. Lett. **25**, 734 (1970).

[76] Ph. Ghosez, J. P. Michenaud, and X. Gonze, Phys. Rev. B **58**, 6224 (1998).

[77] R. Comes, S. M. Shapiro, B. C. Frazer, and G. Shirane, Phys. Rev. B **24**, 1559 (1981).

[78] W. N. Lawless, C. F. Clark, and S. L. Swartz, Ferroelectrics Lett. **44**, 121 (1982).

[79] I. H. Ismailzade, R. M. Ismailov, and A. I. Alekberov, Ferroelectrics **31**, 165 (1981).

[80] D. Wagner and D. Baurle, Ferroelectrics **45**, 295 (1982).

[81] I. H. Ismailzade, Ferroelectrics **45**, 296 (1982).